THE KINEMATICS OF THE SAGITTARIUS STREAM

by

Thomas Gentry Brink

A dissertation submitted in partial fulfillment
of the requirements for the degree of
Doctor of Philosophy
(Astronomy and Astrophysics)
in The University of Michigan
2014

Doctoral Committee:

Professor Mario L. Mateo, Chair
Professor Nuria P. Calvet
Professor Timothy A. McKay
Assistant Professor Kelly Holley-Bockelmann, Vanderbilt University

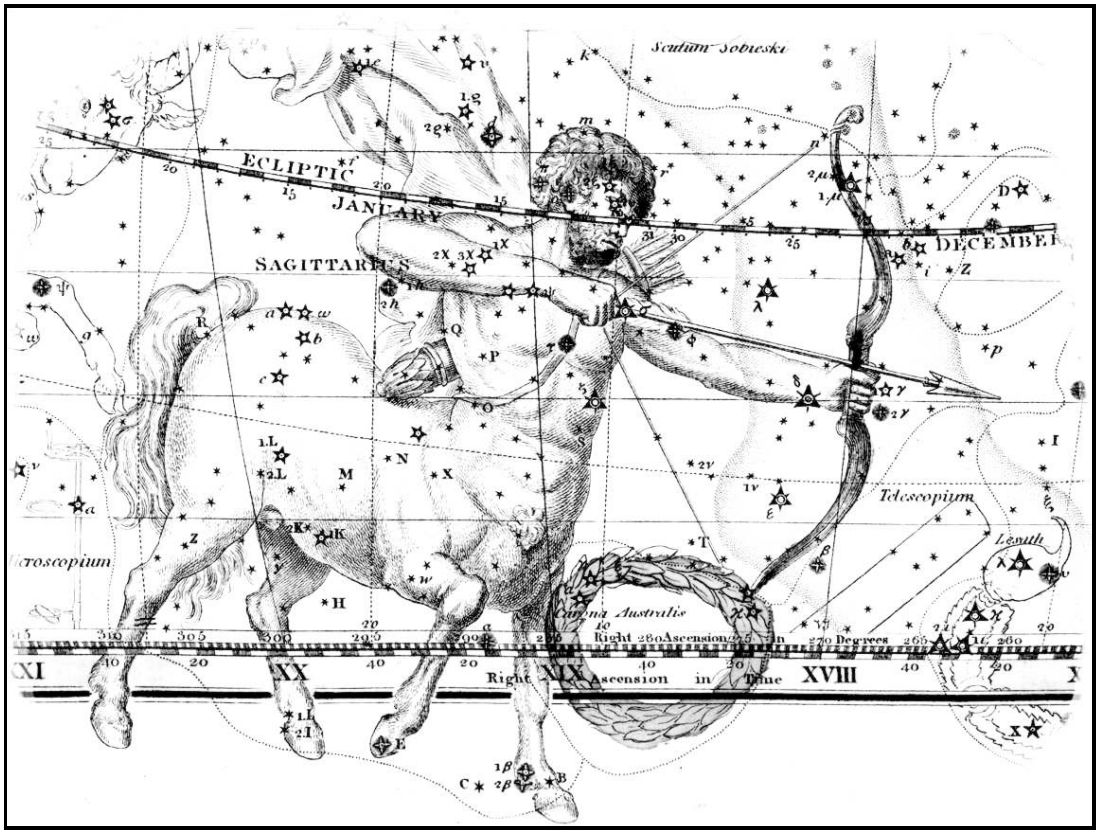
Scutum Sobieski
ECLIPTIC
JANUARY
DECEMBER
SAGITTARIUS
Telescopium
Lenuth
Corona Australis
Right Ascension in Time
Right Ascension in Degrees
XI
XX
XIX
XVIII

Copyright © Thomas Gentry Brink 2014
All Rights Reserved

For my love, Christina.

Your eternal support and unconditional love make everything possible.

The Antennae Galaxies (NGC 4038 & NGC 4039) and their tidal dwarf galaxy (NGC 4038S)

ACKNOWLEDGMENTS

Convention dictates that the student be listed as the sole author on the title page of their dissertation. The truth is that this dissertation, like those that came before it, would have never come to fruition without the help and support of many, many kind people. If I can't give them all the "front page" credit they deserve, the least I can do is use this space to properly acknowledge the generous contributions they have made, and attempt to convey my gratitude to them.

First and foremost, I need to thank my advisor, Mario Mateo. He has taught me, to put it simply, how to be a scientist. He has allowed me the time to experiment, to make mistakes, and to learn from those experiences. He has always been patient, understanding, generous with his time, and fair. In Mario I found both a scientific mentor, and a teaching mentor as well. Over the course of my graduate career I have developed a true passion for teaching, and no one has more greatly influenced my style and approach to teaching than Mario. I will always be indebted to Mario for all that he has done for me.

I also need to express my deep gratitude to my committee members Nuria Calvet, Kelly Holley-Bockelmann, and Timothy McKay, for their continuous support and guidance throughout my graduate career. Their many helpful comments and suggestions have improved the quality of this dissertation immensely. I also want to thank

Kelly for graciously hosting me at Vanderbilt University, and generously spending a week of her time sharing her modeling expertise with me. I am especially grateful to Nuria, who, throughout her term as the graduate student advisor, and later as a member of my thesis committee, provided the advocacy, support, and motivation I needed to finally get across the finish line.

Over the years I have had productive collaborations with David Martínez-Delgado. I thank him for his help and contributions, and also for hosting an excellent winter school in the Canary Islands, which was both intellectually stimulating and highly enjoyable.

I also need to acknowledge the Astronomy department's tremendous support staff, both past and present, whose tireless and often behind-the-scenes efforts I have greatly benefited from. I especially want to recognize everything that Brian Cox has done for me since his arrival four years ago, and particularly over the last year. I am also greatly appreciative of the administrative support provided by Jan Malaikal, Carin Scott, and Sarah Lloyd, the computer support provided by Jeremy Hallum and Roy Bonser, and the teaching support provided by Shannon Murphy. I thank our Department Chair, Joel Bregman, for his continued support throughout the final few years of my thesis work. I also want to thank our graduate advisor, Jon Miller, for helping to provide the motivation I needed to get through the challenging final year of work on my thesis.

The Rackham Graduate School has been an amazing resource throughout my time here. They have provided assistance of all types, on issues big and small. I particularly

want to recognize the tremendous work of Darlene Ray-Johnson, who was a tireless advocate on my behalf, and without whom none of this would have been possible. I will forever be grateful to Darlene for everything she has done for me. I also wish to thank Michael Solomon, the Associate Dean for Academic Programs and Initiatives, for providing tuition support during my final year.

The work presented in this dissertation relied above a massive amount of observational data, requiring approximately twenty trips to astronomical observatories in both hemispheres. I quickly fell in love with observing, and always anxiously looked forward to the next trip, so I could experience the thrill of operating a world-class telescope again. The support I have received at each observatory has been absolutely superb. I thank all of the support staff at Las Campanas Observatory for making each of my twelve trips there enjoyable. I especially want to thank my friend, Mauricio Martínez, for showing us around his home city of La Serena, Chile, and for many hours of pleasant conversation during the long nights on the mountain. I want to express my gratitude to Héctor Balbotín, and the rest of the culinary staff at Las Campanas, for specially preparing so many delicious vegan meals for me. I also wish to thank John Thorstensen, Bob Barr, and the rest of the MDM staff for their help during my six trips to the MDM Observatory. I was fortunate enough to observe once at the MMT Observatory, where Perry Berlind and Mike Calkins expertly controlled the two robotic fiber positioners necessary to acquire data with Hectospec. I also owe a big thanks to Nelson Caldwell for providing much needed assistance with `XFITFIBS`

during the planning stages before our run, and also for deftly managing the MMT observing queue throughout the semester.

During my time in the Astronomy department I have been fortunate to befriend a number of postdocs and research scientists. Jimmy Irwin and I have had productive collaborations on a number of research projects. More importantly, Jimmy has been a great friend for many years. I have enjoyed the time we've spent playing tennis and racquetball, discussing sports, complaining about life, and laughing. I thank Jimmy for always being willing to listen, and for being a true friend when I needed one the most. I need to thank Chris Mullis and David Berger for enthusiastically listening to my complaints regarding the many design flaws in my coffee mug during Friday Tea each week. I thank Sébastien Maret for generously spending hours of his time helping me with my new computer, and I thank Renato Dupke for just being Renato Dupke. Joanna and Julie also deserve a tremendous amount of credit for helping me navigate through the rough waters, and land ashore safely.

Getting through graduate school was extremely difficult, to say the least, and I never could have done it without the help, support, and friendship of my fellow graduate students. I consider myself supremely fortunate to have met, and shared an office with the brilliant Ajay Tannirkulam. From Ajay I have learned so much about so many things – I can't even begin to make a list. His optimism is infectious, and his kindness is unequaled. Although Ajay has returned to his native India after graduating, I truly hope our paths cross again in the future – sooner rather than later.

I thank Matt Walker for helping with many aspects of my research over the years. He was exceedingly generous with his time, and always seemed to have the perfect solution to whatever problem I was facing – which is probably why I pestered him so frequently. I also thank Matt for his tacit acknowledgement of the inferiority of baseball relative to all other sports. I thank Javier Alonso-García for his patience when trying to teach me Spanish one word at a time, for being a great companion on the numerous trips we took together, and for teaching me an important life lesson: never trust a Spaniard with your pudding. I thank Joe Bernstein for the many thought provoking conversations we have had, often times at the intersection of sports and statistics. I thank Jess Werk for finally figuring out how to use COSMOS, and for her distinguished service on the Noble Air Hockey Tournament Committee. I always enjoyed spending a few evenings each winter yelling at the atrocious CCHA referees (especially Molina), and discussing the bimodality of Al Montayo's performances with the other die-hard Michigan Hockey fans: Sarah Ragan, Jess Krick, and Becky Stanek. I thank Matt Greco for being the only person in the department who shared my love of college basketball, and my obsession with the NCAA tournament. I thank Ming Zhao for being such a kind and helpful friend, and for the many great conversations we've had. I thank Julia Plummer for her help early in my graduate career, specifically with all things related to teaching. I thank Mike Richard for the many great conversations and debates. I also need to thank my classmate, Rebecca Billmeier, for persevering through the first two years with Ajay and me – we made a pretty good team.

I offer a special thanks to all four of my grandparents, who continue to inspire me every day – especially to my grandmother Jenny Lou Brink, who has always encouraged me to reach for the stars. Without the love and support of my parents, Tim and Pam Brink, and my sister, Carolyn Brink, I could never have reached this point in my life. I thank you from the bottom of my heart for the lifetime of sacrifices you've made. Over the last few years I have been constantly motivated to earn my doctorate before my Uncle earned his. Though I may have finished in second place, I thank Dr. Uncle John (Jack-Bone[1]) Brink, LL.D. for providing the continuous motivation and encouragement necessary for me to finally get across the finish line. I also wish to thank Jared Avigliano and Michael Flores – the two best friends anyone could ever hope to have.

Most importantly, I need to thank my amazing wife, Christina Brink. Without her love, patience, support, encouragement, understanding, and sacrifice this never could have happened. I hope she can take as much satisfaction it its completion as I do, because she most certainly deserves to! Finally, two years ago our daughter, Bianca Brink, was born. One of the things I've learned in the limited experience I have as a father, is that while raising children we are frequently too preoccupied with how we are positively impacting their development to realize how they are positively impacting ours. Bianca has brought so much joy to our lives. Though she doesn't realize it, she has been highly motivational during these final two years. Sometimes just seeing the sparkle in her eye, a smile upon her face, or hearing her one of a kind

[1]Two points of clarification: (1) There is, in fact, no "Bone" in his name, and (2) After taking (1) in to consideration, this is his name, and he kindly requests that you refrain from wearing it out.

laugh was all I needed to persevere a little while longer. My thanks and my love go out to Bianca, and to all of my family, immediate and extended, for everything.

CONTENTS

LIST OF FIGURES

Figure

LIST OF TABLES

Table

LIST OF ABBREVIATIONS

2MASS	Two Micron All Sky Survey
BHB	Blue Horizontal Branch (stars)
BS	Blue Stragglers
BTC	Big Throughput Camera
CCD	Charge-Coupled Device
ccdf	complementary cumulative distribution function
cdf	cumulative distribution function
CMD	Color-Magnitude Diagram
COSMOS	Carnegie Observatories System for Multi-Object Spectroscopy
CTIO	Cerro Tololo Inter-American Observatory
GSR	Galactic Standard of Rest
IMACS	Inamori-Magellan Areal Camera and Spectrograph
IRAF	Image Reduction and Analysis Facility
K-S	Kolmogorov–Smirnov (test)
LCO	Las Campanas Observatory
lsr	local-standard-of-rest
MDM	Michigan-Dartmouth-MIT (Observatory)
MMT	Multiple Mirror Telescope (Observatory)

QUEST	QUasar Equatorial Survey Team
RGB	Red Giant Branch (stars)
RRL	RR Lyrae (stars)
SDSS	Sloan Digital Sky Survey
SEGUE	Sloan Extension for Galactic Understanding and Exploration
SEKBO	Southern Edgeworth-Kuiper Belt Object (Survey)
Sgr	Sagittarius
USNO	United States Naval Observatory
VES	Virgo Equatorial Stream
VOD	Virgo Overdensity
VSS	Virgo Stellar Stream
WFC	Wide Field Camera

ABSTRACT

Tidal streams can provide us with a great deal of information about their dwarf progenitors, and by implication, the progenitors of the building blocks of stellar halos, such as: their stellar populations, their mass and mass loss rate, and their orbital history and future. But, perhaps more importantly, streams can help us probe properties of their host galaxy. Since the locations, and motions of the stars that comprise a stream reflect the underlying gravitational potential in which they orbit, their positions and kinematics can be used to determine, or at least place constraints upon, the distribution of matter in the halo. In particular, the size and shape of the dark matter halo can be constrained.

There have been numerous efforts to use observations of the Sgr streams to constrain the shape of the Milky Way's dark matter halo. Sgr is the only known Milky Way satellite with substantial streams encircling more than 360° around its host, making it the perfect candidate for such a study. However, various models, relying upon the contemporaneously available observations of Sgr, have produced strikingly contradictory results, initiating a seemingly intractable debate over the shape of the Milky Way's dark matter halo. The data has been interpreted in favor of halos of all possible shapes: spherical, oblate, prolate, triaxial, and transitional.

We present the results of an extensive observational undertaking to acquire the single largest spectroscopic data set of Sgr stream stars. Using a combination of telescopes and instruments in both hemispheres we have completed a kinematic survey including velocity measurements for 2368 unique main-sequence stars in 39 fields spanning the full 360° along the Sgr streams.

The results of this kinematic survey are compared to the predictions of N-body models of the destruction of Sgr in Galactic halos of various shapes. We find that the observed radial velocity trends along the streams are best reproduced by the triaxial halo model. Amongst the axisymmetric models, the prolate halo provides the best match to the observations, while the spherical and oblate models can be ruled out.

CHAPTER 1

Introduction

1.1 Streams as Probes of the Halo Potential

Within the framework of hierarchical structure formation the stellar halos of large galaxies are assembled via a perpetual process of gravitational acquisition, subsequent disintegration, and eventual amalgamation of smaller primordial stellar systems. Ancient accretion events account for the smooth stellar halo, whose constituents have circumnavigated their new host galaxy under the gravitational influence of its dark matter halo for a sufficiently long time ($\sim$10 Gyr) as to become well-mixed in all six dimensions of phase-space (Bullock & Johnston, 2005). In addition to the smooth halo component there exists a variety of substructure that has survived to the present epoch, including: dwarf galaxies, globular clusters, ultra-faint satellites, and the scattered remnants of disrupted stellar systems. These scattered remnants often have the appearance of streams of stars arcing through their host galaxy's halo as they remain, for a little while longer, coherent structures in both position and velocity space.

Though these low surface brightness stellar debris streams have eluded detection until recently, they are now being discovered in the halos of the Milky Way (Majewski et al., 2003; Belokurov et al., 2006), Andromeda (Ibata et al., 2001a, 2007), and

even galaxies outside of the local group (Martínez-Delgado et al., 2008, 2009, 2010; Miskolczi et al., 2011) with regularity. These detections have been greatly aided by the advent of contemporary wide-area imaging surveys, specifically the Two Micron All Sky Survey (2MASS) and the Sloan Digital Sky Survey (SDSS). To date, the quintessential example of stellar debris streams are those belonging to the Sagittarius dwarf spheroidal galaxy (Sgr).

In the course of an investigation in to the kinematics and chemical abundances of stars on the outskirts of the Galactic Bulge, a low-dispersion highly-anomalous velocity structure was detected in three fields spanning 8° in Galactic latitude (Ibata et al., 1994, 1995). These authors had serendipitously uncovered the kinematic signature of Sgr, which had heretofore eluded detection – obscured from view behind the Galactic bulge. At 24 kpc from the Sun and with a galactocentric distance of just 16 kpc, Sgr is the closest confirmed dwarf galaxy to the Milky Way.

When dwarf galaxies, like Sgr, venture in to the depths of their hosts' gravitational potential well the consequences are dire and the prognosis is grim. Gravitational tidal forces due to the host galaxy cause the body of the dwarf to become severely distorted from its original shape, allowing stars once gravitationally bound to the dwarf to escape. Some stars will escape with slightly smaller galactocentric distances than the core of the dwarf, and will thus have slightly shorter Keplerian orbital periods around the host galaxy. Over time these stars will advance further and further in front of the dwarf galaxy, forming a leading stream of tidal debris. Likewise, other stars will escape with slightly larger galactocentric distances than the core of the

dwarf, and will thus have slightly longer Keplerian orbital periods around the host galaxy. Over time these stars will lag further and further behind the dwarf galaxy, forming a trailing stream of tidal debris.

Tidal streams can provide us with a great deal of information about their dwarf progenitors, and by implication, the progenitors of the building blocks of stellar halos, such as: their stellar populations, their mass and mass loss rate, and their orbital history and future. But, perhaps more importantly, streams can help us probe properties of their host galaxy. Since the locations, and motions of the stars that comprise a stream reflect the underlying gravitational potential in which they orbit, their positions and kinematics can be used to determine, or at least place constraints upon, the distribution of matter in the halo. In particular, the size and shape of the dark matter halo can be constrained.

There have been numerous efforts to use observations of the Sgr streams to constrain the shape of the Milky Way's dark matter halo. Since Sgr is the only known Milky Way satellite with substantial streams encircling more than 360° around its host, it is not just the perfect candidate, but also the only candidate for such a study. However, various models, relying upon the contemporaneously available observations of Sgr, have produced strikingly contradictory results, initiating a seemingly intractable debate over the shape of the Milky Way's dark matter halo. The data has been interpreted in favor of halos of all possible shapes: spherical (Ibata et al., 2001c; Fellhauer et al., 2006; Ibata et al., 2013), oblate (Martínez-Delgado et al., 2004; Johnston et al., 2005; Law et al., 2005; Martínez-Delgado et al., 2007), prolate

(Helmi, 2004b; Law et al., 2005), triaxial (Law et al., 2009; Law & Majewski, 2010; Deg & Widrow, 2013), and transitional (Vera-Ciro & Helmi, 2013).

In this dissertation we present the results of an extensive observational undertaking to acquire the single largest spectroscopic data set of Sgr stream stars. Our kinematic survey covered 39 fields that span the entire 360° extent of the streams. The addition of this valuable study to the panoply of existing observations of Sgr will help to shed a little more light on the dark halo of our galaxy and one of its most enigmatic inhabitants.

1.2 Studies of the Sgr Streams

The Sgr streams have been an area of active research for nearly twenty years. Throughout that time many significant observations and theoretical advances have been made. However, as more has been learned about the streams and the halo in which they evolve, new questions and contradictions continue to surface. In this section a chronological review of the relevant literature is provided. Of particular significance to this dissertation are the observational studies that have determined the positions and measured the velocities of newly found Sgr tidal debris, and the N-body models of the destruction of Sgr that these observations help to constrain. It is on these two methods of inquiry that the following literature review focuses. First, to provide some useful background, we begin with a brief summary detailing a typical way in which the Sgr–Milky Way system is modeled as an N-body system of particles orbiting in a static, three-component potential.

1.2.1 Modeling the Destruction of Sgr

Since its discovery (Ibata et al., 1994, 1995), many researchers have attempted to model the destruction of Sgr due to the gravitational tidal forces exerted on it by the Milky Way. Most efforts model the predisruption dwarf as a pressure supported N-body system with particles distributed according to a Plummer sphere (Plummer, 1911):

$$\Phi_{\mathrm{Sgr},0}(r) = -\frac{GM_{\mathrm{Sgr},0}}{\sqrt{r^2 + r_p^2}}, \tag{1.1}$$

where $M_{\mathrm{Sgr},0}$ represents the initial mass of Sgr, r_p represents its Plummer radius, and G is the gravitational constant. These parameters are usually allowed to vary within the models, with typical ranges of $M_{\mathrm{Sgr},0} = 10^7 - (5 \times 10^9)\ M_\odot$ and $r_p = 0.2 - 1.5$ kpc. A King profile (King, 1966) has also been frequently used to model the initial particle distribution within Sgr. The King model, which does not have an analytic form, can be fully specified with three parameters: the King radius, r_0, which defines the radius at which the local density has fallen to about half of the central density, the central velocity dispersion, σ_0, and Ψ_0/σ_0^2, which characterizes the how centrally concentrated the distribution is in terms of the ratio of the central value of the relative potential, Ψ_0, to the square of the central velocity dispersion. Typical values assumed for these parameters when modeling Sagittarius are: $r_0 \sim 0.5$ kpc, $\sigma_0 \sim 15 - 30$ km s^{-1}, and $\Psi_0/\sigma_0^2 \sim 3.3$.

The Galactic potential in which the orbiting Sgr system is allowed to evolve is

typically assumed to be static and to consist of three independent components: a Miyamoto & Nagai disk (Miyamoto & Nagai, 1975), Hernquist spheroid (Hernquist, 1990), and an axisymmetric logarithmic halo. These three components can be expressed analytically in cylindrical coordinates (R, z) as follows:

The gravitational potential of the disk takes the form:

$$\Phi_{\rm disk}(R,z) = -\frac{GM_{\rm disk}}{\sqrt{R^2 + (a + \sqrt{z^2 + b^2})^2}}, \tag{1.2}$$

where $M_{\rm disk}$, a, and b represent the mass of the Milky Way's disk and its radial and vertical scale lengths, respectively. These parameters are typically assigned values of $M_{\rm disk} = 1.0 \times 10^{11}\ M_\odot$, $a = 6.5$ kpc, and $b = 0.26$ kpc.

The gravitational potential due to the spheroid can be written:

$$\Phi_{\rm sphere}(R,z) = -\frac{GM_{\rm sphere}}{\sqrt{R^2 + z^2} + c}, \tag{1.3}$$

where $M_{\rm sphere}$ and c represent the mass of the Milky Way's spheroid and its scale radius, respectively. These parameters are typically assigned values of $M_{\rm sphere} = 3.4 \times 10^{10}\ M_\odot$ and $c = 0.7$ kpc. Note that $\sqrt{R^2 + z^2}$ is just the spherical radial coordinate r.

Finally, the axisymmetric gravitational potential due to the Milky Way's halo can be expressed as:

$$\Phi_{\rm halo}(R,z) = \frac{1}{2} v_{circ}^2 \ln \left[R^2 + \left(\frac{z}{q} \right)^2 + d^2 \right], \tag{1.4}$$

where d represents the scale size of the halo, which is usually assigned a typical value of $d = 12$ kpc, but has been allowed to vary in some models. The parameter v_{circ} represents the asymptotic value for the velocity of a circular orbit in the disk under the influence of the combined gravitational potential of the Milky Way:

$$\Phi_{\rm MW}(R,z) = \Phi_{\rm disk} + \Phi_{\rm sphere} + \Phi_{\rm halo}. \tag{1.5}$$

The dimensionless parameter q defines the flattening of the halo as the ratio of the gravitational equipotentials. This ratio is defined as the equipotential along the axis perpendicular to the disk (i.e. the z direction) relative to the equipotential along an axis in the plane of the disk. Note that since axisymmetry is assumed, the equipotentials along both axes in the plane of the disk (x and y) are identical. With the halo flattening defined in this manner, it follows that a spherical halo is the special case where ($q = 1$), and oblate and prolate halos are described by ($q < 1$) and ($q > 1$) respectively. The determination of the optimal value for q is often the principal goal of the modeling efforts. To this end, numerous models are typically generated with q values ranging from $\sim 0.8 - 1.5$ in an effort to see which value best produces the observed velocities and three-dimensional positions of the Sgr debris.

1.2.2 Early Work with the Sgr Streams

The first attempts to model the Sgr-MW system primarily sought to use the limited available observational data to constrain the orbit of the dwarf galaxy (Velazquez & White, 1995; Johnston et al., 1995; Ibata et al., 1997; Edelsohn & Elmegreen, 1997; Jiang & Binney, 2000). Some of the dwarf galaxy's observed characteristics that helped guide these early modeling efforts included its location, size, shape, and orientation as well its radial and transverse velocities, velocity dispersion, and radial velocity gradient. Ibata & Lewis (1998) were the first to test models with different values for the halo flattening ($q = [0.9, 1.0]$), but ultimately did not reach a conclusion as to which value the observational data favored. Without the detection of any Sgr debris in the tidal tails, all of the early models lacked the leverage necessary to constrain the shape of the Milky Way's halo.

The first detection of an extended stream of tidally stripped stars emanating from Sgr was made by Mateo et al. (1998). They successfully traced the trailing stream in seventeen fields ranging from $10^\circ - 34^\circ$ from the center of Sgr, and measured the surface density profile across this debris segment. Several subsequent modeling efforts (Gómez-Flechoso et al., 1999; Johnston et al., 1999; Martínez-Delgado et al., 2001; Helmi & White, 2001) succeeded in reproducing the observed surface density profile measurements, however they each assumed only a spherical halo, opting to not test other possible halo shapes.

Ibata et al. (2001c) tested a number of different halo shapes, ranging from oblate

to spherical ($q_\rho{}^1 = [0.50, 0.55, ..., 1.0]$), in an attempt to reproduce the positions, distances, and radial velocities observed for a recently discovered set of 60 halo carbon stars (Totten & Irwin, 1998; Totten et al., 2000). After employing something akin to a sigma-clipping algorithm, the authors concluded that a maximum of 19 of the 60 stars were found to be consistent with any individual model of the disruption of Sgr. Given the high degree of coplanarity of the unrejected stars, whose locations are well fit by a great circle, they found that nearly spherical models ($q_\rho \gtrsim 0.9$) best fit the observations. As the oblateness of the halo is increased (i.e. q_ρ is decreased) the modeled debris is seen to precess across larger swaths of the sky, in opposition to the observations. In a separate contribution (Ibata et al., 2001b) the authors show that their $q_\rho = 0.9$ model can successfully explain the recently identified halo substructure observed in SDSS A stars (Yanny et al., 2000) as tidal debris from Sgr.

Martínez-Delgado et al. (2004) used the same carbon star data as Ibata et al. (2001c), as well as numerous other spectroscopic and photometric detections of Sgr debris, to help constrain the shape of the the Milky Way's halo. They modeled a wide range of oblate halo density distributions ($q_\rho = [0.1, 0.2, 0.4, 0.5, 0.6, 0.8, 1.0]$) and found the $q_\rho = 0.5$ model, corresponding to a potential flattening of $q = 0.85$, to best match the available observational data.

[1]Note that while q refers to the axis ratio of the gravitational equipotentials, q_ρ, which is a function of the cylindrical coordinates (R, z) for an axisymmetric potential, refers to the axis ratio of the isodensity surface at a specified (R, z) location. Ibata et al. (2001c) define $q_\rho \equiv q_\rho(50 \text{ kpc}, 0)$.

1.2.3 A Clearer Picture Starts to Emerge

A major leap forward was made when the Sgr debris streams were traced across nearly the entire sky using 2MASS M giant candidate stars (Majewski et al., 2003). Long segments of the trailing and leading streams spanning at least 150° and 50°, respectively, were detected (see their Figure 3, for example). They authors fit a great circle to a winnowed set of 695 survey M giants, and used it to define the equator of a new heliocentric spherical Sgr coordinate system, $(\Lambda_\odot, B_\odot)$, which we describe in detail in Section 2.1. However, it is noted that when fitting great circles to the leading and trailing streams independently, they find the two to be inclined to one another at an angle of $\sim$10° due the precession of the debris and the perspective effect of galactocentric parallax. The widths of the streams, measured perpendicular to the orbital plane, are estimated to be $\sim$8 kpc or more, and photometric parallax techniques were used to estimate the distances of the M giants.

Majewski et al. (2003) assert that the qualitative appearance of the streams, specifically the noted lack of significant precession in the locations of the M giant debris, implies a nearly spherical halo potential. However, Helmi (2004a) caution against concluding (as Majewski et al. (2003) and Ibata et al. (2001c) did) that debris displaying a high degree of coplanarity necessarily implies a spherical halo, as the observed Sgr debris is likely to have been stripped from the dwarf within the last $\sim$3 Gyr, which may be too recent for it to have experienced the precession-inducing effects of a flattened halo. To support their claim, Helmi (2004a) produced a series of models with varying halo flattenings ($q = [0.80, 0.90, 1.00, 1.11, 1.25]$), and carefully

chosen initial conditions, to demonstrate that the available observations of Sgr debris were consistent with a wide range of halo shapes.

Follow up spectroscopy was obtained for a subset of 284 of the 2MASS M giant candidates (Majewski et al., 2004). The chosen stars were required to be within 6.3 kpc of the Sgr debris plane defined by Majewski et al. (2003). The vast majority (90%) were located along the trailing tidal tail, ranging from 25°–150° from the center of Sgr. Of these, 89 were kinematically confirmed members of the trailing Sgr stream.

Law et al. (2004) presented radial velocities for an additional sample of about 130 2MASS M giant candidates along the leading stream, ranging from 185°–330° from the center of Sgr. Of these, 94 stars, spanning 230°–330° from the center of Sgr, were kinematically confirmed members of the leading Sgr stream (Law et al., 2005).

This combined photometric and spectroscopic study of 2MASS M giants, which provided three-dimensional positions (Majewski et al., 2003) and radial velocities (Majewski et al., 2004; Law et al., 2005) along most of the Sgr debris plane, produced the first extensive observational data beyond the central region of Sgr, and thus provided substantial new constraints for the next generation of models of the disruption of Sgr.

The first models to incorporate the M giant radial velocity measurements were published by Helmi (2004b) using the same five halo models as originally described in Helmi (2004a; i.e. $q = [0.80, 0.90, 1.00, 1.11, 1.25]$). They found that the radial velocities measured along the trailing stream, which consists of debris that was stripped from the main body relatively recently ($\lesssim$1.6 Gyr ago), could be adequately repro-

duced by all five halo shapes (though the most oblate model, with $q = 0.8$, slightly outperformed the others). The kinematics of the leading stream, however, which consists of older debris that was stripped from the main body $\lesssim$4 Gyr ago, provided much more stringent constraints on the halo's shape. The leading stream radial velocities strongly favored a prolate ($q \geq 1.25$) shape for the Milky Way's halo, marking the first instance that observational data was interpreted to favor an elongated over a flattened halo potential.

Johnston et al. (2005) used the M giant data in an entirely different way, and ultimately arrived at a completely contradictory result. Rather than investigate the constraints imposed by the newly acquired velocities, they focused solely on the three-dimensional positions of the M giants. They constructed a series of models with a broad range of halo flattenings ($q = [0.80, 0.85, ..., 1.45]$), each with initial conditions carefully chosen to best reproduce the M giant positional and kinematic data. For the M giant data and for each of their models, the authors determined the best-fit planes to the three-dimensional positions of the stars/particles in the leading and trailing Sgr streams independently. The orientations of these best-fit debris planes can be concisely defined by the galactic coordinates of their orbital poles. The locations of the leading and trailing stream orbital poles, and the angular offset between them, can then be used to characterize the direction and degree of precession exhibited by the stars/particles in the data and the models.

Johnston et al. (2005) found that the location of the orbital pole of the trailing stream was essentially model-independent, but the location of the leading stream's

orbital pole was highly sensitive to the halo flattening parameter, q. This result is not unexpected, as the trailing stream contains debris that has not been unbound from the main body of Sgr long enough to experience the effects of precession, while the leading stream, which contains older debris, has had sufficient time to precess. The degree and direction of precession observed in the leading stream is best matched by the slightly oblate halo model with $q = 0.90$. They rule out halos with $q < 0.85$ and $q > 1.05$ at the 3σ level. The prolate model inferred from the leading stream radial velocities (Helmi, 2004b), with $q = 1.25$, actually causes the debris to precess in the opposite direction as observed, and is ruled out at the 5σ level.

This presents a clear contradiction between the preferred halo models as inferred from the leading stream M giants' positions (i.e. oblate) and their velocities (i.e. prolate). Johnston et al. (2005) argue in favor of their orbital pole precession measurements, which they claim are almost exclusively influenced by the shape of the underlying gravitational potential, while there are a number of additional effects that can alter the kinematics within the tidal streams.

Law et al. (2005) executed a series of simulations, constrained by the M giant data set, that explored a wide range of parameter space in order to determine the best-fit models with three different halo flattenings: $q = 0.90, 1.00, 1.25$. They ultimately reached the same conclusions as Helmi (2004b) and Johnston et al. (2005): that only the prolate halo is capable of reproducing the observed velocities in the leading stream, and that only the oblate halo can reproduce the observed precession of the orbital plane. They conclude that this discrepancy implies that the orbit of Sgr must

have evolved over the time period probed by the data (∼3 Gyr). It is worth noting that in a welcome departure from established precedent, Law et al. (2005) have made available the full results of the 10^5 particles in each of their three best fit models. This is of great value to the community as the results not only help to inform and guide new and ongoing observational programs, but they also greatly facilitate quantitative comparisons between the models and the observational data.

1.2.4 Bifurcations in the Stream

Belokurov et al. (2006), using upper main-sequence and turnoff stars from the fifth data release of the SDSS (Adelman-McCarthy et al., 2007), uncovered a bifurcation in the leading stream of Sgr. The bifurcation, which appears as two parallel arcs stretching ∼50° across the celestial sphere, consists of a dominant "A" branch and secondary "B" branch offset by ∼9° to higher declinations. The B branch lies very close to the best-fit Sgr debris plane derived from the 2MASS M giants (Majewski et al., 2003). They also report the possible existence of additional Sgr debris, possibly associated with a wrap of the Sgr stream, behind the A branch. A qualitative comparison with the models of Helmi (2004a), based on the breadth of the debris on the sky, leads the authors to conclude that their observations appear most consistent with the model halos satisfying $1.0 \lesssim q < 1.1$.

Fellhauer et al. (2006) was the first to offer a potential explanation for the observed bifurcation. They attempted to model the bifurcation in simulations with a wide range of halo flattenings ($q = [0.80, 0.90, 0.95, 1.00, 1.05, 1.11, 1.25, 1.50]$) and found that the observed bifurcation could only be reproduced with appropriate initial

conditions (i.e. Sgr mass and proper motion) and a spherical halo potential ($q = 1$). This model interprets the A and B branches as young leading and old trailing Sgr debris, respectively. The weakly detected third branch, located behind the A branch, is predicted by this model to be old leading debris, and is referred to as the C branch. The model also predicted the existence of a fourth branch of young trailing debris behind the B branch, which is referred to as the D branch. Given the very low degree of precession indicated by the small angular offset between the A/C branches and the B/D branches, and the facts that the A and C branches and the B and D branches overlap one another, the authors conclude that strongly oblate and prolate halos must be ruled out. The authors also clearly demonstrated the importance of adopting an appropriate value for the initial mass of Sgr. Masses that are too high ($M_{\rm Sgr,0} \gtrsim 5 \times 10^8 M_\odot$) produce a high velocity dispersion in the predisruption dwarf, causing the stripped Sgr debris to quickly become very broad across the sky, washing out the appearance of two distinct stellar streams. From this analysis they conclude that the initial mass of Sgr must be less than $5 \times 10^8 M_\odot$.

1.3 Overview of the Dissertation

Despite the great progress that has been made in studying the Sgr streams, both observationally and theoretically, it is clear that many questions remain, and contradictions abound. This dissertation is an attempt to further unravel the mysteries of Sgr and the dark halo that has been tearing it apart.

Using a combination of telescopes and instruments in both hemispheres we have completed a kinematic survey in 39 fields spanning the full 360° along the Sgr streams.

Table 1.1: Kinematic Studies of the Sgr Streams

Study	Population	$N_{\rm Stars}$	$\Lambda_\odot$	σ_V (km s^{-1})
Majewski et al. (1999)	Red Clump	30	27°	12
Ibata et al. (2001c)	Carbon Stars	60	Full Range	10
Dohm-Palmer et al. (2001)	RGB[a] stars	21	300°–30°	20
Kundu et al. (2002)	K giants	8	266°–308°	5
Yanny et al. (2003)	SDSS BHBs[b] & BS[c]	119	109°	7
Majewski et al. (2003)	2MASS M giants	89	25°–150°	6
Law et al. (2004, 2005)	2MASS M giants	94	232°–332°	6
Monaco et al. (2007)	2MASS M giants	67	30°–100°	0.5
Yanny et al. (2009)	SDSS M giants/BHBs	55/999	60°–140°/190°–300°	12
Ruhland et al. (2011)	SDSS BHBs	70	255°–295°	11

Note: $N_{\rm stars}$ refers to the number of kinematically confirmed Sgr members when stated by the authors, otherwise it refers to the number of candidates. The typical velocity measurement uncertainty in given in the σ_V column.
[a] Red Giant Branch stars
[b] Blue Horizontal Branch stars
[c] Blue Stragglers

In each field we obtained V and I band photometric images from which we selected probable halo main-sequence stars as candidates for spectroscopic follow-up. Main-sequence stars offer several key advantages over other potential tracers of tidal stream debris. First, they greatly outnumber stars in other evolutionary stages[2]. This feature more readily allows for positive detections of the streams to be made in all of our fields, some of which may lack other tracers. Also, the richer kinematic sampling in any given field yields better statistics. Additionally, because main-sequence stars are longer-lived than other populations[3] they can be used to trace older portions of the streams, stripped from their dwarf progenitor long ago. Simulations have shown (as discussed in Section 1.2) that the older debris has the greatest potential to discriminate between the various halo models.

[2]Main-sequence stars outnumber M giants, for example, by about 500:1.

[3]M giants, for example, have expected lifetimes of only 2–3 Gyr.

Chapter 2 summarizes the photometric component of this survey. First, an explanation of how the fields were chosen and the unique heliocentric Sgr coordinate system that describes their locations is provided. This is followed by a description of the various instruments, and instrumental setups, used to acquire the necessary V and I band images. We then summarize the data reduction process that ultimately produced instrumental magnitudes and equatorial coordinates for every point source in all fields. After an explanation of how candidate main-sequence stars were selected from $(I, V-I)$ instrumental color-magnitude diagrams, the process of properly calibrating the photometry is described in detail. At the end of Chapter 2 the dereddened color-magnitude diagrams, including the candidate selection box locations, are presented for all fields.

Spectroscopic follow-up in these fields was accomplished primarily with the Inamori-Magellan Areal Camera and Spectrograph (IMACS) on the Baade telescope at the Las Campanas Observatory (LCO). For a short segment of the Sagittarius stream located at (relatively) high declinations ($\delta \gtrsim 25^{\circ}$) we obtained spectra with the multi-fiber spectrograph Hectospec on the MMT telescope at the MMT Observatory (MMTO).

In Chapter 3 we summarize the spectroscopic component of this survey. We begin with a thorough discussion of the IMACS spectroscopy, followed by a similar discussion of the Hectospec spectroscopy, and conclude by providing a full analysis of the velocity measurement uncertainties and estimated errors in the combined data set. In the IMACS section we first describe the instrumental setup and the process by which the IMACS mutli-slit masks were designed. A summary of all of the IMACS

spectroscopic observations is then provided along with a description of the unique observing sequence. Next, a detailed accounting of the data reduction steps that ultimately produced wavelength calibrated, continuum subtracted, one-dimensional spectra is given. The IMACS section then concludes with an explanation of how the radial velocity of each object spectrum is measured using a Fourier cross-correlation technique.

The Hectospec section of Chapter 3 proceeds, in general, in the same way as the IMACS section. It begins with a description of the instrumental setup and the process by which the fibers are assigned to stellar targets. This is followed by a summary of the completed observations and a description of the observing sequence. Finally, a detailed discussion of the data reduction steps and velocity measurement procedure is given.

In the final section of Chapter 3 a full analysis of the velocity measurement uncertainties is presented. First, repeat observations are used to determine the uncertainties in each instrument's velocity measurements. Next, the repeat observations are investigated more closely, revealing a modest uncorrectable systematic velocity offset in the repeated IMACS fields. Our velocity measurements are then compared to existing velocity measurements in the SDSS (for IMACS and Hectospec) and in the radial velocity standard field SA57 (for Hectospec). Chapter 3 concludes with a brief discussion of the multiple steps taken to winnow the data set by excluding stars with unreliable velocity measurements. Tables listing the coordinates and relevant

photometric and kinematic information for every star in every field are included at the end of Chapter 3.

In Chapter 4 we present a case study in which we apply our methods to a single, high interest field. We obtained multi-slit radial velocity measurements for 111 stars in the direction of the Virgo Stellar Stream (VSS). The stars were photometrically selected to be probable main-sequence stars in the Galactic halo. Some oblate models for the shape of the Milky Way's dark matter halo predict that the leading arm of the Sgr stream should pass through this volume, and have highly negative radial velocities ($V_{\rm gsr} \lesssim$ –200 km s^{-1}), as it descends down from the northern Galactic hemisphere towards the Galactic plane (Martínez-Delgado et al., 2004; Law et al., 2005; Martínez-Delgado et al., 2007). To test this hypothesis, we constructed our observed radial velocity distribution for this field, and compared it to the predictions of these models, the more recent triaxial halo model of Law & Majewski (2010), and the expected velocity of the VSS. From these comparisons we then discuss the likelihood that Sgr debris is present in this volume of the halo, and if so, which halo shape our observations prefer. The data and analysis presented in Chapter 4 was previously published in *The Astronomical Journal* (Brink et al., 2010).

In Chapter 5 we describe how the velocity distribution profiles and their 95% confidence bounds are created. The velocity distribution profiles are then shown for every field. The primary and secondary peak velocities in each field are identified, marked on their corresponding figure, and listed in an included table. A pair of new statistics that provide two distinct ways to assess the asymmetry in each velocity

distribution profile are then defined and calculated. We then introduce and describe the four models (oblate, prolate, spherical, and triaxial) whose predictions we later test against our survey results. To test the models we compare the peak velocities observed in each of our fields with the radial velocity predictions they make.

In Chapter 6 we first provide a brief summary of the important topics and results covered in each chapter of this dissertation. We then detail the most significant conclusions that can be drawn from this study. Specifically, we discuss what this kinematic survey of Sgr reveals about the nature of the streams, and how the current models of the destruction of Sgr compare with our results. Finally, we conclude with a look towards the future, by describing the observational and theoretical limitations of the present, and how they can be overcome, to ultimately improve our understanding of the Sgr streams and the halo that produced them.

CHAPTER 2

Photometric Observations

2.1 Data Acquisition

The spectroscopic component of this survey was principally conducted with IMACS (Dressler et al., 2011) on the 6.5 m Baade telescope at the Las Campanas Observatory (LCO). Before acquiring stellar spectra it is first necessary to select candidate stars for spectroscopic follow-up. To select suitable candidates we acquired V and I band imaging in many fields along the Sgr streams. We used the best-fit Sgr plane of Majewski et al. (2003, see their §5.2), with a slight modification, to guide us in selecting the locations of our fields. The Sgr debris path we adopted is, like the Majewski et al. (2003) path, a great circle on the sky, but with the additional constraint that the path must pass through the location of the main body of the Sgr dwarf. The Majewski et al. (2003) path, derived from 2MASS M-giant candidates, does not come within $1\overset{\circ}{.}5$ of the main body of Sgr. We chose locations along this path with typical field-to-field separations of 5° to 15°, excluding two larger gaps near where the Galactic plane crosses the Sgr debris plane. Additionally, due to the uncertainty in the true path of the streams and its breadth on the sky, data was also acquired in fields 2° above and/or below the nominal stream path at some stream locations.

Table 2.1 lists the coordinates of our fields in various systems: equatorial ($\alpha_{J2000.0}$, $\delta_{J2000.0}$), galactic (l,b), and the Sagittarius coordinate system ($\Lambda_\odot$,$B_\odot$). The first column of Table 2.1 specifies the designated name of each field. Each field's name is derived from its coordinates in the Sagittarius coordinate system (Majewski et al., 2003), which is a heliocentric, spherical coordinate system. The Sgr debris plane defines the equator of this system, and the zero-point of the longitudinal coordinate, $\Lambda_\odot$, coincides with the center of the main body of Sgr. This coordinate increase from 0° to 360° in the direction of the trailing debris stream, which coincides with the general direction in which right ascension increases. The latitudinal coordinate in the Sgr coordinate system, $B_\odot$, is defined to be zero along the Sgr debris plane, and to increase up to ±90° at the system's poles. The northern and southern Sgr hemispheres are defined to contain their corresponding galactic coordinate counterparts. The naming convention adopted for our fields combines each field's Sgr longitude followed by its Sgr latitude. These two coordinates are separated by a "p" or an "n" representing the sign of the Sgr latitude. Table 2.1 also provides the galactic extinctions (in magnitudes), A_V and A_I, calculated using the maps of Schlegel et al. (1998). Plots are provided showing the locations of the observed fields in the equatorial (Figure 2.1), galactic (Figure 2.2), and Sgr (Figure 2.3) coordinate systems.

2.1.1 Imaging for IMACS Spectroscopy

The majority of the imaging used to select these candidate stars for spectroscopic follow-up with IMACS was also obtained with IMACS operating in its direct imaging mode. Table 2.2 summarizes relevant properties of these V and I band photometric

Table 2.1: Field Coordinates in Various Systems

Field	$\alpha_{J2000.0}$	$\delta_{J2000.0}$	l	b	$\Lambda_\odot$	$B_\odot$	A_V	A_I
000.1n01.5	18 55 21	–30 28 17	5.642	–14.144	0.081	–1.475	0.52	0.31
010.1n03.2	19 41 17	–33 23 58	6.357	–24.291	10.115	–3.177	0.55	0.32
020.1n06.1	20 29 37	–36 28 46	5.675	–34.639	20.108	–6.052	0.15	0.09
020.5p00.1	20 30 35	–30 20 04	12.978	–33.529	20.521	0.083	0.24	0.14
060.0p00.6	23 22 24	–21 16 15	44.211	–68.905	59.994	0.572	0.10	0.06
060.1n01.3	23 25 45	–23 01 46	40.137	–70.197	60.057	–1.349	0.09	0.05
075.0p00.9	0 19 27	–14 52 06	90.066	–75.658	74.976	0.854	0.09	0.05
075.1n01.1	0 23 23	–16 33 02	89.944	–77.587	75.071	–1.074	0.08	0.05
090.0n00.7	1 16 55	–9 11 38	142.678	–71.082	90.037	–0.747	0.10	0.06
090.0p01.3	1 12 45	–7 25 19	138.300	–69.655	90.009	1.302	0.42	0.25
090.1n02.7	1 21 05	–10 53 59	147.615	–72.335	90.092	–2.738	0.10	0.06
105.1n02.3	2 12 30	–3 00 36	165.209	–59.058	105.090	–2.329	0.10	0.06
119.9p00.0	2 59 04	6 27 04	170.233	–44.386	119.903	–0.021	0.66	0.39
135.1p00.5	3 52 07	14 13 28	175.284	–29.748	135.069	0.505	1.22	0.71
139.9n07.6	4 24 44	9 07 07	185.562	–26.911	139.945	–7.629	1.15	0.67
147.0n04.5	4 45 32	14 52 04	183.851	–19.397	147.007	–4.526	1.96	1.15
150.0n01.1	4 51 18	19 14 41	181.028	–15.680	150.014	–1.057	1.35	0.79
150.0n08.9	5 03 45	11 56 54	189.050	–17.446	149.962	–8.945	0.99	0.58
177.4n02.7	6 46 40	25 54 44	189.089	10.524	177.375	–2.663	0.37	0.22
180.4n11.2	7 05 39	18 02 07	198.249	11.165	180.380	–11.176	0.18	0.10
197.4n00.9	8 15 55	29 34 52	192.858	30.266	197.359	–0.897	0.12	0.07
198.4n10.9	8 20 00	19 32 22	204.096	27.945	198.367	–10.931	0.13	0.08
207.1p00.2	9 00 59	30 08 06	195.054	39.882	207.083	0.170	0.09	0.05
215.1p00.8	9 37 58	29 35 36	197.772	47.675	215.095	0.769	0.06	0.04
222.2n09.1	9 59 40	18 29 34	215.970	49.688	222.227	–9.089	0.09	0.05
224.9p01.1	10 22 03	27 43 56	203.076	56.975	224.931	1.132	0.13	0.08
235.1p01.8	11 06 18	25 11 18	211.673	66.374	235.139	1.761	0.05	0.03
245.0p01.3	11 45 23	21 05 26	231.221	73.783	245.004	1.338	0.07	0.04
246.8n05.9	11 40 15	13 45 22	248.218	68.674	246.822	–5.873	0.13	0.08
250.1p01.2	12 04 50	18 53 13	248.065	76.489	250.075	1.235	0.07	0.04
255.0n00.9	12 19 29	14 51 43	270.107	75.656	254.987	–0.856	0.12	0.07
255.1p03.1	12 27 27	18 22 03	269.463	79.645	255.117	3.133	0.09	0.06
256.7n04.1	12 19 50	11 12 35	276.396	72.433	256.689	–4.089	0.10	0.06
260.0p01.0	12 41 24	14 12 51	292.163	76.876	260.002	0.984	0.11	0.06
265.0p00.9	12 59 23	11 46 24	310.256	74.532	265.019	0.908	0.09	0.06
275.1p00.6	13 34 19	6 36 25	331.267	67.089	275.061	0.635	0.11	0.07
285.0p00.3	14 08 10	1 19 26	341.633	58.308	285.012	0.326	0.12	0.07
295.0p00.0	14 42 10	–4 00 30	347.830	48.968	295.034	0.026	0.31	0.18
305.0n00.2	15 16 30	–9 12 28	352.059	39.447	305.018	–0.246	0.29	0.17
315.1n00.6	15 51 52	–14 20 17	355.143	29.712	315.071	–0.632	0.54	0.31

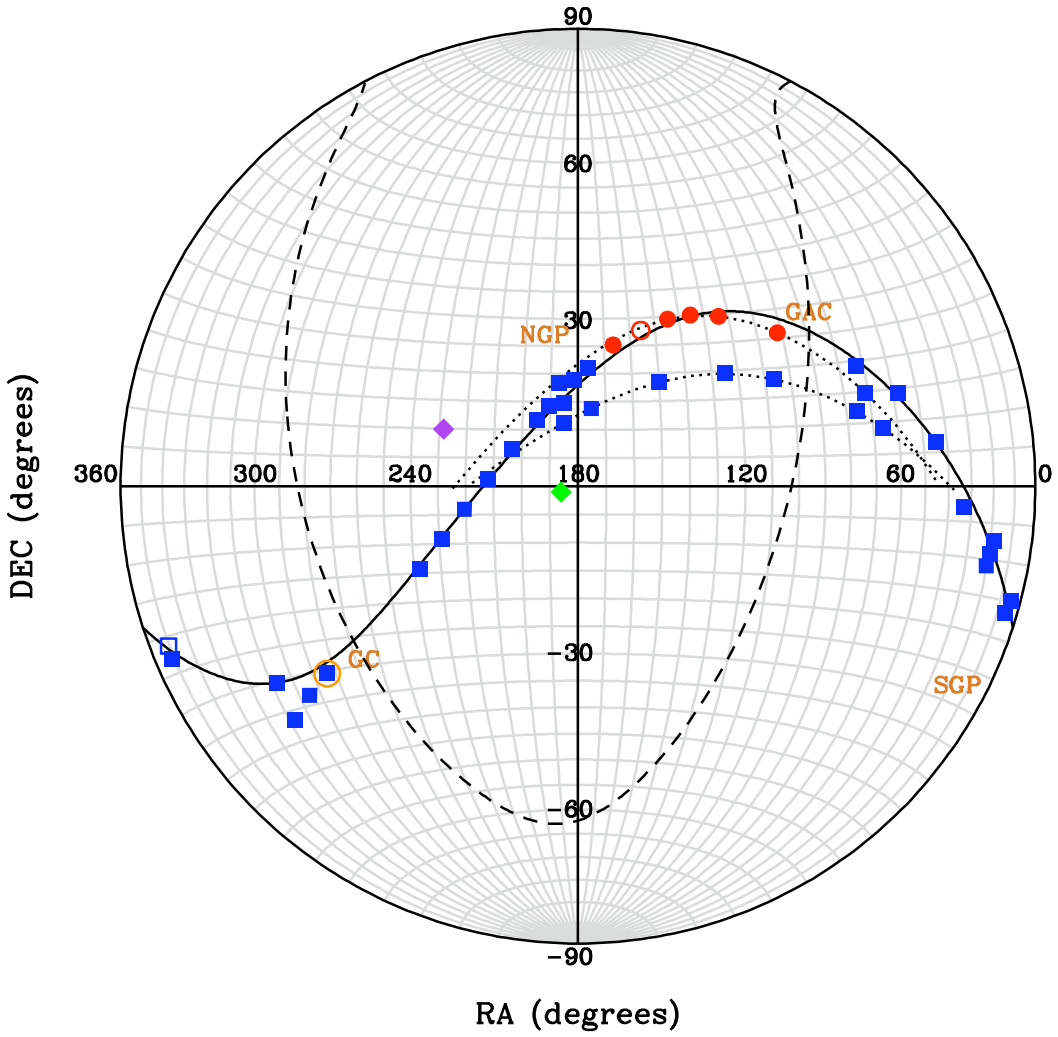

Figure 2.1: Field map in the equatorial coordinate system. The equatorial coordinates of the IMACS (blue squares) and Hectospec (red circles) fields are plotted. The center of the Sgr dwarf is designated with an open orange circle. The Sgr debris plane as defined by Majewski et al. (2003) is designated by a solid black line. The path of the Galactic plane is indicated with a dashed line, and the locations of the Galactic center (GC), anticenter (GAC), north Galactic pole (NGP) and south Galactic pole (SGP) are all labeled. The paths of the bifurcations (Belokurov et al., 2006) are marked with dotted lines. Additionally, the Virgo and Virgo control fields discussed in Chapter 4 are denoted by a green and purple diamond respectively. The open square and circle represent the IMACS and Hectospec fields in which data was acquired but, because of poor weather (IMACS) and astrometry (Hectospec), was immediately discarded.

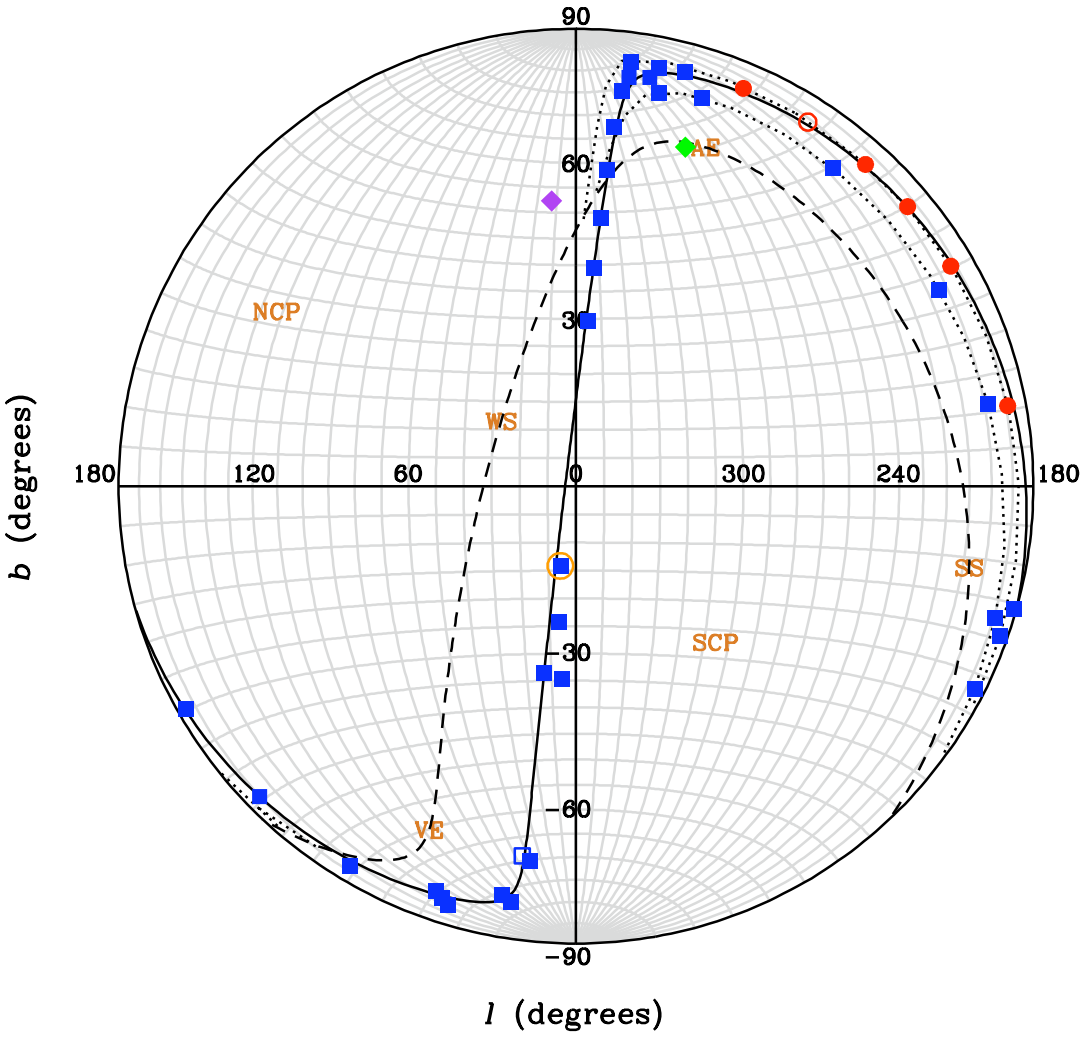

Figure 2.2: Field map in galactic coordinates. The galactic coordinates of the IMACS (blue squares) and Hectospec (red circles) fields are plotted. The center of the Sgr dwarf is designated with an open orange circle. The Sgr debris plane as defined by Majewski et al. (2003) is designated by a solid black line. The path of the celestial equator is indicated with a dashed line, and the locations of the vernal equinox (VE), summer solstice (SS), autumnal equinox (AE), winter solstice (WS), north celestial pole (NCP) and south celestial pole (SCP) are all labeled. The paths of the bifurcations (Belokurov et al., 2006) are marked with dotted lines. Additionally, the Virgo and Virgo control fields discussed in Chapter 4 are denoted by a green and purple diamond respectively. The open square and circle represent the IMACS and Hectospec fields in which data was acquired but, because of poor weather (IMACS) and astrometry (Hectospec), was immediately discarded.

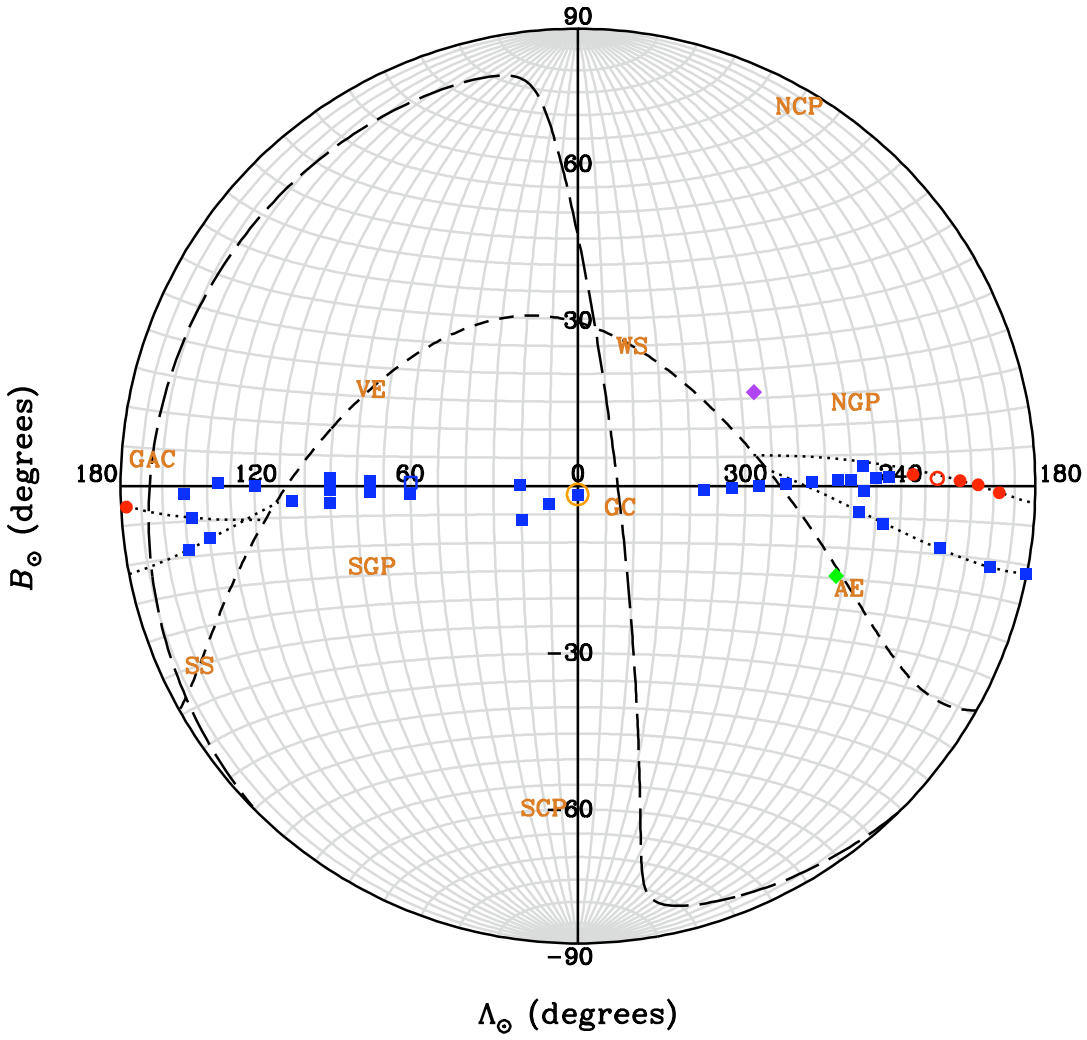

Figure 2.3: Field map in the Sagittarius coordinate system. The Sagittarius coordinates (Majewski et al., 2003) of the IMACS (blue squares) and Hectospec (red circles) fields are plotted. The center of the Sgr dwarf is designated with an open orange circle. The path of the Galactic plane is indicated by the long-dashed line, and the locations of the Galactic center (GC), anticenter (GAC), north Galactic pole (NGP) and south Galactic pole (SGP) are all labeled. The path of the celestial equator is indicated by the short-dashed line, and the locations of the vernal equinox (VE), summer solstice (SS), autumnal equinox (AE), winter solstice (WS), north celestial pole (NCP) and south celestial pole (SCP) are also labeled. The paths of the bifurcations (Belokurov et al., 2006) are marked with dotted lines. Additionally, the Virgo and Virgo control fields discussed in Chapter 4 are denoted by a green and purple diamond respectively. The open square and circle represent the IMACS and Hectospec fields in which data was acquired but, because of poor weather (IMACS) and astrometry (Hectospec), was immediately discarded.

observations. The first column of Table 2.2 specifies the designated name of each field as described above. The second column in Table 2.2 lists the date of the observations, which range from 2006 June through 2006 November. The third and fourth columns provide the V band and I band exposure times, respectively, which are either 240 seconds in V and 150 seconds in I, or 360 seconds in V and 240 seconds in I. The remaining columns list the galactic extinctions and the airmass' for both the V and the I filter images. These images were all taken at low to moderate airmass' of $X \lesssim 1.65$.

These direct images were all taken with IMACS in the $f/4.3$ configuration. The $f/4.3$ camera consists of eight 2K $\times$ 4K CCD detectors combined to form a 8K $\times$ 8K mosaic. This provides for a $15\farcm4 \times 15\farcm4$ field of view, and when binned 2×2 produces a spatial resolution of $0\farcs222$ pixel^{-1}.

For six of our IMACS spectroscopic fields the images from which we selected candidates were not taken with IMACS. For these fields we used a combination of three different instruments. Table 2.3 summarizes the relevant properties of these photometric observations, such as the instrument used, the date of the observation, and the exposure times, galactic extinctions, and airmass' in both the V and I filters.

Three of these six fields were imaged with the 8K CCD mosaic on the 2.4 m Hiltner telescope at the Michigan-Dartmouth-MIT (MDM) Observatory. Like IMACS, the MDM 8K consists of eight 2K $\times$ 4K CCD detectors combined to form a 8K $\times$ 8K mosaic. However, for all of these observations one of the corner CCDs, identified as

Table 2.2: Summary of Imaging with IMACS for IMACS Spectroscopy

Field	UT Date	ET_V(s)	ET_I(s)	A_V	A_I	X_V	X_I
000.1n01.5	2006 Jun 20	240	150	0.52	0.31	1.15	1.16
060.0p00.6[a]	2006 Jun 20	240	150	0.10	0.06	1.06	1.06
060.1n01.3	2006 Jun 19	240	150	0.09	0.05	1.01	1.01
075.0p00.9	2006 Jun 20	240	150	0.09	0.05	1.11	1.12
075.1n01.1	2006 Jun 19	240	150	0.08	0.05	1.05	1.05
090.0p01.3	2006 Jun 19	240	150	0.42	0.25	1.41	1.43
090.0n00.7	2006 Jun 20	240	150	0.10	0.06	1.15	1.16
090.1n02.7	2006 Jun 20	240	150	0.10	0.06	1.36	1.35
105.1n02.3	2006 Jun 20	240	150	0.10	0.06	1.48	1.50
119.9p00.0	2006 Sep 20	360	240	0.66	0.39	1.29	1.28
135.1p00.5	2006 Sep 20	360	240	1.22	0.71	1.38	1.39
139.9n07.6	2006 Nov 29	360	240	1.15	0.67	1.43	1.45
147.0n04.5	2006 Nov 30	360	240	1.96	1.15	1.59	1.59
150.0n01.1	2006 Sep 21	300	200	1.35	0.79	1.50	1.50
150.0n08.9	2006 Nov 29	360	240	0.99	0.58	1.43	1.42
180.4n11.2	2006 Nov 29	360	240	0.18	0.10	1.48	1.47
198.4n10.9	2006 Nov 29	360	240	0.13	0.08	1.62	1.64
245.0p01.3	2006 Jun 19	240	150	0.07	0.04	1.58	1.59
250.1p01.2	2006 Jun 19	240	150	0.07	0.04	1.51	1.51
255.0n00.9	2006 Jun 20	240	150	0.12	0.07	1.43	1.44
255.1p03.1	2006 Jun 19	240	150	0.09	0.06	1.50	1.49
260.0p01.0	2006 Jun 20	240	150	0.11	0.06	1.40	1.40
265.0p00.9	2006 Jun 20	240	150	0.09	0.06	1.34	1.35
275.1p00.6	2006 Jun 20	240	150	0.11	0.07	1.24	1.25
285.0p00.3	2006 Jun 20	240	150	0.12	0.07	1.16	1.16
295.0p00.0	2006 Jun 20	240	150	0.31	0.18	1.10	1.10
305.0n00.2	2006 Jun 20	240	150	0.29	0.17	1.10	1.11
315.1n00.6	2006 Jun 20	240	150	0.54	0.31	1.05	1.04

[a] Field 060.0p00.6 was eventually removed from the data set because of problems with the spectroscopy.

Table 2.3: Summary of Additional Imaging for IMACS Spectroscopy

Field	Instrument	UT Date	ET_V(s)	ET_I(s)	A_V	A_I	X_V	X_I
010.1n03.2	CTIO4m+BTC	1998 Jul 1	900	720	0.55	0.32	1.42	1.50
020.1n06.1	CTIO4m+MosaicII	1999 Sep 18	900	600	0.15	0.09	1.08	1.10
020.5p00.1	CTIO4m+MosaicII	1999 Sep 18	900	600	0.24	0.14	1.00	1.01
222.2n09.1	MDM2.4m+8K	2007 May 19	3x1200	3x1200	0.09	0.05	1.28	1.66
246.8n05.9	MDM2.4m+8K	2007 May 20	3x1200	3x1200	0.13	0.08	1.42	1.92
256.7n04.1	MDM2.4m+8K	2007 May 19	3x1200	3x1200	0.10	0.06	1.85	1.37

chip number "3", was not functioning. The 8K has a field of view of $24\farcm0 \times 24\farcm0$, and when binned 2×2 produces a spatial resolution of $0\farcs36$ pixel^{-1}.

Two of the fields were imaged with the Mosaic II camera on the 4 m Blanco telescope at the Cerro Tololo Inter-American Observatory (CTIO). Like IMACS and the MDM 8K, the Mosaic II consists of eight 2K × 4K CCD detectors combined to form a 8K × 8K mosaic. The Mosaic II has a field of view of $36\farcm8 \times 36\farcm8$, and a spatial resolution of $0\farcs27$ pixel^{-1}.

A single field was imaged with the Big Throughput Camera (BTC) on the 4 m Blanco Telescope at CTIO. The BTC consists of four 2K × 2K CCD detectors combined to form a 4K × 4K mosaic. It has a field of view of $34\farcm8 \times 34\farcm8$, but with fairly large $5.5'$ gaps between each of the four CCDs. The BTC has a spatial resolution of $0\farcs27$ pixel^{-1}.

2.1.2 Imaging for Hectospec Spectroscopy

The Sagittarius streams are observed to stretch from a declination of $\sim -35°$ in the southern hemisphere, near the main body of the dwarf, up to $\delta \sim 30°$ in the northern hemisphere (see Figure 2.1). In the northern hemisphere the Sgr stream apparently bifurcates in to a lower declination "A" branch and a higher declination "B" branch

(Belokurov et al., 2006). The more prominent A branch apparently reaches its peak declination near (α, δ) $\sim$ (135°, 20°). Data presented by Belokurov et al. (2006) suggests that most of the stars that comprise the B branch have $150° \lesssim \alpha \lesssim 210°$, but that if the orbital path of the B branch is extrapolated it would reach its highest declination near (α, δ) $\sim$ (135°, 30°). With IMACS located at the Las Campanas Observatory in Chile, at a latitude of 29° S, it is impractical to use it to obtain multi-slit spectroscopy for $\delta \gtrsim 20°$. Therefore, we used the multi-fiber spectrograph Hectospec, located at the MMT Observatory in southern Arizona, to acquire spectroscopy in six high-declination fields along the B branch.

The projected path of the B branch on the sky very nearly overlaps with the projected path of the Majewski et al. (2003) best-fit Sgr debris plane. In choosing the locations for these six fields we used a combination of the Majewski et al. (2003) path and the path of the B branch as revealed by the Belokurov et al. (2006) study of upper main-sequence and turnoff stars in the Sloan Digital Sky Survey (SDSS) data set. Additionally, the three of our six fields that are furthest to the west, and just to the east of the Galactic plane, near the Galactic anticenter, were selected by extrapolating a great circle fit to the Belokurov et al. (2006) B Branch.

In order to select candidates for spectroscopic follow-up we first obtained imaging of these six fields that lie along the approximate path of the B branch of the bifurcation and its extrapolation. These fields are spaced about 10° apart, and have declinations in the range $25° \lesssim \delta \lesssim 30°$. For three of the six fields we acquired the necessary imaging with the Mosaic II CCD imager on the 4 m Blanco telescope at CTIO.

The $36\farcm8 \times 36\farcm8$ field of view of the Mosaic II CCD imager is fairly well matched to the large 1° diameter field of view of Hectospec. Thus, it was not necessary to tile the three fields imaged with the Mosaic II in order to cover a suitable area of the sky from which to select candidates for spectroscopic follow-up. These fields were all imaged in 2007 December for 480 seconds in both the V and I filters. Given the declination of the targets relative to the latitude of CTIO, and other priorities on that particular observing run, it was necessary to perform these observations at relatively high airmass' of $X \sim 2.0$. These observations are summarized near the bottom of Table 2.4.

For the remaining three fields we acquired the necessary imaging with the 8K CCD array on the 2.4 m Hiltner telescope at the MDM Observatory. The field of view of the MDM 8K CCD array ($24\farcm0 \times 24\farcm0$) is significantly smaller than the 1° diameter field of view of Hectospec. We therefore sought to tile each of the three MDM fields with imaging in four contiguous subfields to provide us with an effective area of $48' \times 48'$ from which to select spectroscopic candidates. Unfortunately, due to poor weather we were only able to acquire imaging in three out of four subfields for one of the three MDM fields. These observations took place between 2006 February and 2008 February. Throughout these observations a corner CCD, identified as chip number "3", in the 4×2 array of CCDs in the 8K detector was not operational. All imaging was done with the V and I filters. For all 11 subfields we obtained three 1200 s exposures in V. For five of the subfields we obtained three 900 s exposures in I, for another five we obtained three 1200 s exposures in I, and for one field we

Table 2.4: Summary of Imaging for Hectospec Spectroscopy

Field	Subfield	Instrument	UT Date	ET_V(s)	ET_I(s)	A_V	A_I	X_V	X_I
207.1p00.2	1	MDM2.4m+8K	2008 Feb 11	3×1200	3×1200	0.09	0.05	1.20	1.54
207.1p00.2	2	MDM2.4m+8K	2007 Nov 13	3×1200	3×900	0.09	0.05	1.25	1.33
207.1p00.2	3	MDM2.4m+8K	2007 Nov 19	3×1200	3×900	0.09	0.05	1.22	1.39
207.1p00.2	4	MDM2.4m+8K	2008 Feb 13	3×1200	3×1200	0.09	0.05	1.19	1.45
215.1p00.8	1	MDM2.4m+8K	2006 Mar 3	3×1200	3×1200	0.06	0.04	1.05	1.00
215.1p00.8	2	MDM2.4m+8K	2008 Feb 10	3×1200	3×1200	0.06	0.04	1.34	1.14
215.1p00.8	3	MDM2.4m+8K	2007 Nov 18	3×1200	4×900	0.06	0.04	1.05	1.01
215.1p00.8	4	MDM2.4m+8K	2008 Feb 12	3×1200	3×1200	0.06	0.04	1.36	1.14
235.1p01.8	1	MDM2.4m+8K	2007 May 21	3×1200	3×900	0.05	0.03	1.24	1.50
235.1p01.8	2	MDM2.4m+8K	2007 Nov 13	3×1200	3×900	0.05	0.03	1.37	1.23
235.1p01.8	3	MDM2.4m+8K	2007 Nov 17,19	3×1200	3×900	0.05	0.03	1.27	1.30
177.4n02.7	···	CTIO4m+MosaicII	2007 Dec 18	480	480	0.37	0.22	1.96	2.00
197.4n00.9	···	CTIO4m+MosaicII	2007 Dec 17	480	480	0.12	0.07	2.06	2.03
224.9p01.1[a]	···	CTIO4m+MosaicII	2007 Dec 18	480	480	0.13	0.08	2.01	2.05

[a] Field 224.9p01.1 was eventually removed from the data set because of problems with the spectroscopy.

acquired four 900 s exposures in I. The images were taken at comparatively lower airmass' of $X \lesssim 1.6$. This information is summarized in Table 2.4.

2.2 Data Reduction and Candidate Selection

All of the imaging, from all instruments, was reduced using standard IRAF[1] procedures. The `ccdproc` task was used to accomplish the initial processing steps. First, the overscan bias level was determined, then subtracted, and finally trimmed from all frames. Next, the `zerocombine` task was used to create a master bias image by averaging together all zero-second exposures taken over the course of each observing run. This master bias frame was then subtracted from all other frames using `ccdproc` again. For the final initial processing step twilight flats in each filter were properly scaled and combined using `flatcombine` to form master twilight flats, which were then divided into all other images taken with the corresponding filter.

[1]IRAF is distributed by the National Optical Astronomy Observatory, which is operated by the Association of Universities for Research in Astronomy, Inc., under cooperative agreement with the National Science Foundation.

For the fields imaged with the MDM2.4m+8K, which had three exposures taken in each filter, it was necessary to properly align each chip in each exposure with the corresponding chips in the other exposures before combining them. To accomplish this, one of the three images was selected as the reference image, and the task `imalign` was used to determine the average two-dimensional shift in pixel coordinates, calculated using several stars per chip, between each chip in the reference image and the corresponding chips in the remaining two images. After these shifts are applied, the images were then averaged together using the task `imcombine` along with the "avsigclip" cosmic ray rejection algorithm.

The next processing step was to determine the instrumental magnitudes of the point sources in each field. The two-dimensional stellar photometry program `DoPHOT` (Schechter et al., 1993) was implemented to measure the instrumental I and V magnitudes of the stars in each field. The `DoPHOT` program also executes an algorithm to determine the two-dimensional centroid position of each identified source, and returns their (x,y) pixel positions along with their instrumental magnitudes to the user. Figure 2.4 plots the uncertainties in the instrumental I magnitude measurements, as reported by `DoPHOT`, as a function of the calibrated, dereddened I magnitude for three fields spanning a range of stellar densities (see the figure caption for more details, and see the following section for details on the calibration process). A representative color-magnitude diagram (CMD) (of the field depicted in the middle panel of Figure 2.4) is shown in Figure 2.5. The I magnitude uncertainties for our candidate stars (see

below for more on the selection process) typically ranged from a few hundredths to $\sim$0.10 magnitudes, with very few higher than that.

The final processing step was to determine the equatorial coordinates of the point sources identified by `DoPHOT` in the previous step. The astrometric transformations from CCD pixel coordinates to equatorial coordinates were performed by the IRAF tasks `msctpeak` and `wcsctran`. First, `msctpeak` is used to match the coordinates of hundreds of stars from the USNO-B1.0 catalog (Monet et al., 2003) to their (x,y) pixel positions on our images. This task was iterated upon two or more times as needed. We found typical rms scatters of $\sim$0$''$.15–0$''$.30 in each field. This scatter is likely dominated by positional uncertainties in the UNSO-B1.0 catalog which is known to include many galaxies and binaries. Once `msctpeak` has determined the transformation equation, the task `wcsctran` applies that equation to the point sources output from `DoPHOT`, resulting in a list of point sources along with their corresponding instrumental magnitudes and equatorial coordinates.

Candidate stars were selected from instrumental (I, $V - I$) color-magnitude diagrams. The selection region was designed to identify probable main-sequence stars in the halo of the Milky Way. We chose stars over a fairly broad color range, and with $I \gtrsim 22.1$ to minimize the possibility of contamination by background galaxies. The selection regions are indicated in each of the CMDs presented at the end of this chapter (Figures 2.10 to 2.19). In addition Table 2.5 lists the boundaries of the boxes used to select Sgr candidate stars and the number of candidates within each box. In an effort to make use of any unused real estate on the IMACS multi-slit

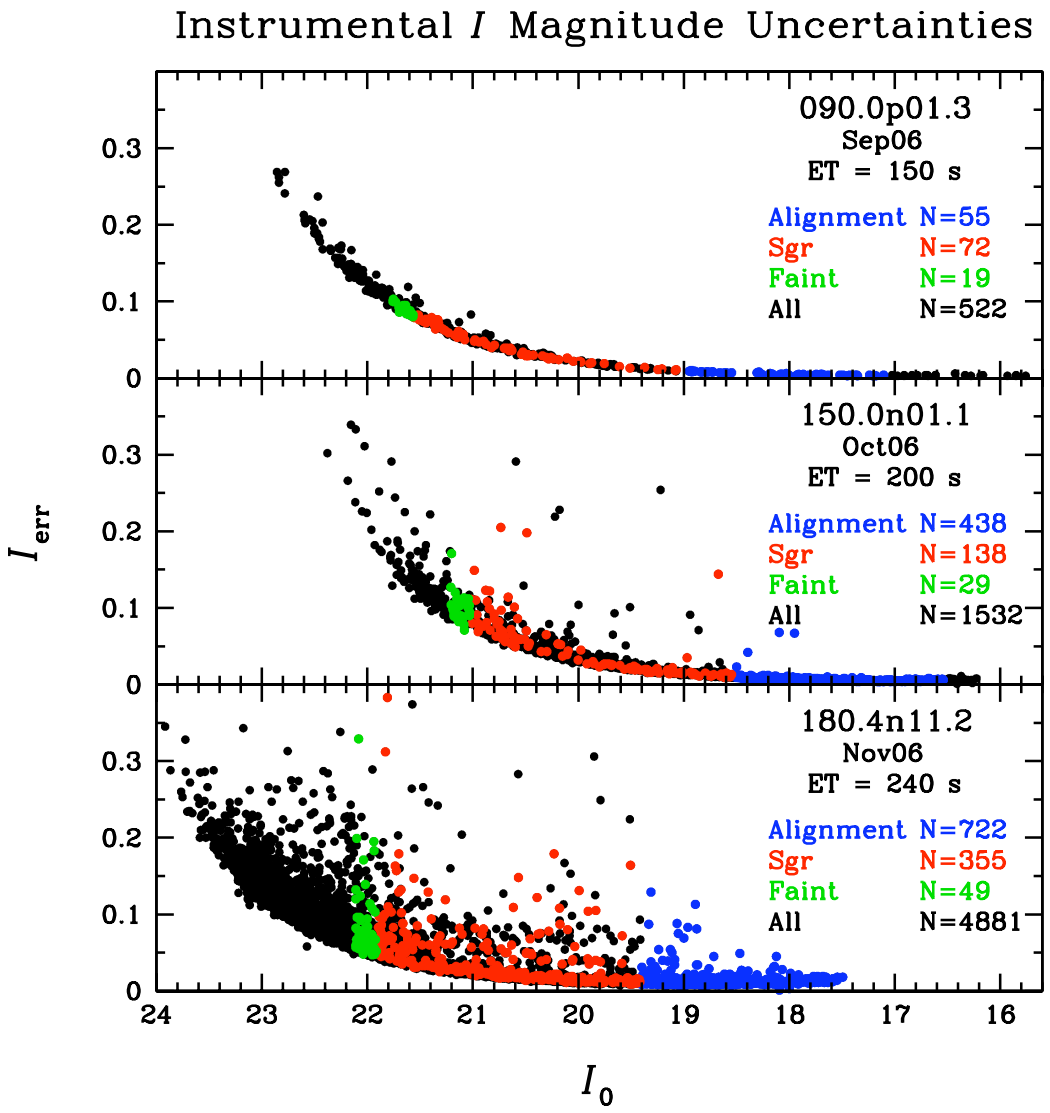

Figure 2.4: Instrumental I magnitude uncertainties for three fields. The instrumental I magnitude uncertainties (as reported by the IRAF task `DoPHOT`) are plotted against the (more informative) calibrated, dereddened I magnitudes, instead of the instrumental magnitudes themselves. Details of the calibration process are discussed in the following section. These fields were chosen because they span a representative range of stellar densities. The field in the top panel is our least dense, the middle panel is of average stellar density (see the CMD in Figure 2.5), and the bottom panel is among the most dense. All three fields were imaged with IMACS during different observing runs: 2006 June, 2006 September, and 2006 November (from top to bottom). They also had three different exposure times: 150 s, 200 s, and 240 s (from top to bottom). The different colored points designate the stars selected as alignment candidates, Sgr candidates, and Sgr faint candidates (as explained below). The numbers of each of these are labeled in each panel along with the total number of point sources, the name of each field, the observing run, and the exposure time. A few stars (1, 1, and 16 from top to bottom) had uncertainties larger than the bounds of the plots.

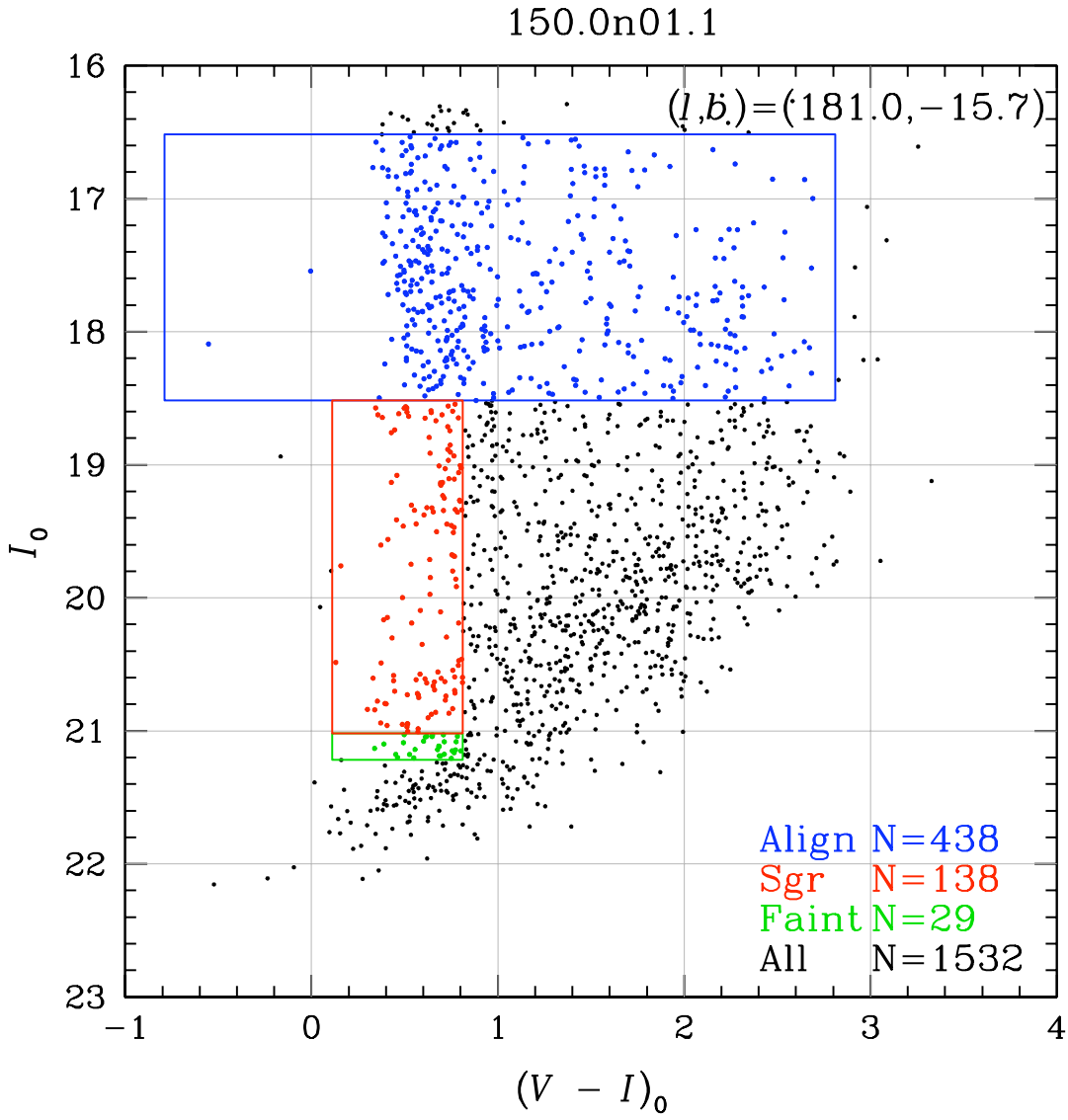

Figure 2.5: Dereddened color-magnitude diagram for a representative field. The instrumental magnitude uncertainties for this field, 150.0n01.1, are plotted in the middle panel of Figure 2.4. Galactic coordinates are shown in the upper right hand corner. Details of the selection boxes are provided below, and details of the calibration process are discussed in the following section.

masks fabricated for spectroscopic follow-up we also selected fainter Sgr candidates. These stars have color ranges identical (or in a few cases very similar) to those of the the standard candidates but extend to slightly fainter magnitudes (typically 0.20 magnitudes fainter than the standard Sgr candidates). The selection boxes for the faint candidates are also indicated in the CMDs at the end of the chapter, and their boundaries and numbers are listed in Table 2.5 as well. For the IMACS spectroscopic fields alignment stars had to be selected to properly align the multi-slit masks on the sky. The regions from which these stars were selected are also indicated on the CMDs at the end of this chapter (Figures 2.10 to 2.19).

2.3 Photometric Calibration

To properly calibrate our photometry we cross-referenced our selected candidate stars against objects in the SDSS data set using a fairly strict constraint on each object's position. We were able to do this directly for the more than half of our fields which are covered by SDSS imaging. For most of the fields not covered by SDSS we were able to calibrate them indirectly using photometric offsets determined from other fields on the same observing run. However, a few of our fields are not covered by SDSS imaging and were not on observing runs with other fields that are covered by SDSS. We attempted to calibrate these fields using stars in the USNO-B1.0 catalog but were unsuccessful. The very few object matches found in the I filter were near the faint limit of the USNO-B1.0 catalog, in an apparently non-linear regime, making them useless for calibration purposes. Additionally, the V filter is not utilized by the USNO-B1.0 catalog. We tried to sidestep this complication by calculating the

Table 2.5: Dereddened CMD Selection Box Locations

Field	$(V-I)_{\rm min}$	$(V-I)_{\rm max}$	$\Delta(V-I)$	$I_{\rm max}$	$I_{\rm min}$	ΔI	$N_{\rm cands}$	$I_{\rm faint}$	$\Delta I_{\rm faint}$	$N_{\rm faint}$
000.1n01.5	0.18	0.88	0.70	21.51	19.01	2.50	20436	21.71	0.20	3147
010.1n03.2[a]	–0.28	0.17	0.45	14.09	12.09	2.00	1016	···	···	···
020.1n06.1[a]	–0.15	0.30	0.45	13.34	11.34	2.00	233	···	···	···
020.5p00.1[a]	–0.18	0.27	0.45	13.30	11.30	2.00	179	···	···	···
060.0p00.6[b]	0.36	1.06	0.70	21.77	19.27	2.50	255	21.97	0.20	69
060.1n01.3	0.37	1.07	0.70	21.77	19.27	2.50	163	21.97	0.20	64
075.0p00.9	0.36	1.06	0.70	21.77	19.27	2.50	141	21.97	0.20	40
075.1n01.1	0.37	1.07	0.70	21.78	19.28	2.50	151	21.98	0.20	53
090.0n00.7	0.35	1.05	0.70	21.76	19.26	2.50	146	21.96	0.20	67
090.0p01.3	0.19	0.89	0.70	21.56	19.06	2.50	72	21.76	0.20	19
090.1n02.7	0.33	1.03	0.70	21.75	19.25	2.50	156	21.95	0.20	51
105.1n02.3	0.32	1.02	0.70	21.75	19.25	2.50	190	21.95	0.20	50
119.9p00.0	0.37	1.07	0.70	21.63	19.13	2.50	218	21.83	0.20	78
135.1p00.5	0.13	0.83	0.70	21.30	18.80	2.50	183	21.50	0.20	53
139.9n07.6	0.17	0.87	0.70	21.34	18.84	2.50	106	21.54	0.20	16
147.0n04.5	0.12	0.82	0.70	20.86	18.36	2.50	176	21.06	0.20	21
150.0n01.1	0.11	0.81	0.70	21.02	18.52	2.50	138	21.22	0.20	29
150.0n08.9	0.23	0.93	0.70	21.43	18.93	2.50	178	21.63	0.20	28
177.4n02.7[c]	–0.03	0.97	1.00	20.11	18.11	2.00	612	···	···	···
180.4n11.2	0.57	1.27	0.70	21.91	19.41	2.50	355	22.11	0.20	49
197.4n00.9	0.06	0.96	0.90	20.26	17.76	2.50	262	···	···	···
198.4n10.9	0.57	1.27	0.70	21.93	19.43	2.50	180	22.13	0.20	60
207.1p00.2	–0.01	1.37	1.38	21.20	16.02	5.18	318	···	···	···
215.1p00.8	0.11	1.27	1.16	21.10	16.50	4.60	289	···	···	···
222.2n09.1[d]	0.25	1.19	0.94	20.30	16.50	3.80	71	20.78	0.48	42
224.9p01.1[b]	0.06	0.96	0.90	20.25	17.75	2.50	166	···	···	···
235.1p01.8	0.23	1.24	1.01	21.16	16.23	4.93	240	···	···	···
245.0p01.3	0.32	1.02	0.70	21.76	19.26	2.50	173	21.96	0.20	50
246.8n05.9[d]	0.23	1.26	1.03	20.65	17.04	3.61	73	21.11	0.46	40
250.1p01.2	0.33	1.03	0.70	21.77	19.27	2.50	92	21.97	0.20	17
255.0n00.9	0.31	1.01	0.70	21.74	19.24	2.50	190	21.94	0.20	17
255.1p03.1	0.32	1.02	0.70	21.75	19.25	2.50	173	21.95	0.20	38
256.7n04.1[d]	0.28	1.14	0.86	20.36	16.47	3.89	81	21.00	0.64	50
260.0p01.0	0.32	1.02	0.70	21.75	19.25	2.50	157	21.95	0.20	35
265.0p00.9	0.33	1.03	0.70	21.76	19.26	2.50	143	21.96	0.20	37
275.1p00.6	0.33	1.03	0.70	21.75	19.25	2.50	149	21.95	0.20	44
285.0p00.3	0.34	1.04	0.70	21.75	19.25	2.50	146	21.95	0.20	39
295.0p00.0	0.27	0.97	0.70	21.64	19.14	2.50	170	21.84	0.20	51
305.0n00.2	0.28	0.98	0.70	21.65	19.15	2.50	200	21.85	0.20	35
315.1n00.6	0.18	0.88	0.70	21.51	19.01	2.50	286	21.71	0.20	36

[a] These three fields could not be photometrically calibrated so we report their instrumental magnitudes and colors.
[b] These two fields were eventually removed from the data set because of problems with their spectroscopy.
[c] A diagonal cut was made along the red edge for field 177.4n02.7 ranging from $(V-I)$ of 0.97 at I of 20.11 to $(V-I)$ of 0.67 at I of 18.11.
[d] The faint candidate selection boxes for these three fields has a different $\Delta(V-I)$ than the Sgr candidate selection boxes and overlap with them due to the fact that the fields were calibrated chip-by-chip after the candidates had already been selected from instrumental CMDs.

quantity $(B + R)/2$ from the USNO-B1.0 results, and then transforming this hybrid magnitude to V. To perform this transformation we chose several of our SDSS-calibrated fields and, for the stars in common between the two surveys, we fit a linear relation between the V magnitude calculated from the g and r SDSS magnitudes (as described below) and the quantity $(B + R)/2$ from USNO-B1.0. We then attempted to use this linear relation to transform from $(B+R)/2$ USNO-B1.0 magnitudes to our instrumental V magnitude. Unfortunately we found this transformation to be much too noisy to be considered reliable, and ultimately decided to just report instrumental magnitudes and colors for these few fields.

Fortunately, nearly all of our fields could be calibrated either directly or indirectly by SDSS. To calibrate our photometry with SDSS data we used the online "CrossID" tool for Data Release 8 (Aihara et al., 2011) or 9 (Ahn et al., 2012), depending on when the calibration was performed. This tool allowed us to upload a file containing the coordinates of our candidate stars in each field, and search their database for the nearest objects within a radius we specified to be $1.8''$. In the fields that overlap the SDSS data set we found matches for nearly all ($\sim 95\%$) of our Sgr candiates, faint candidates, and alignment star candidates within the SDSS database. Our fields typically had 100–200 candidates in them, depending on their galactic latitude. From the SDSS database we pulled the g,r,i,z magnitudes and the star/galaxy "type" classification for all matched objects. Stars which the SDSS had classified as galaxies were immediately removed from the calibration process. In order to calibrate with SDSS data we first needed to convert their magnitudes from the SDSS system to Johnson-

Cousins I and V magnitudes. To accomplish this we applied the transformation equations of Jordi et al. (2006):

$$I_{\rm SDSS} = i - 0.386(i - z) - 0.397 \tag{2.1a}$$

$$V_{\rm SDSS} = g - 0.565(g - r) - 0.016 \tag{2.1b}$$

To correct our instrumental magnitudes ($I_{\rm Inst}$,$V_{\rm Inst}$) for the effects of atmospheric extinction we multiplied the airmass, X, at the time of observation by a filter and site specific extinction coefficient (α_I,α_V), and subtracted that product from our instrumental magnitudes. We used extinction coefficients of 0.04 and 0.14 magnitudes airmass^{-1} in the I and V filters respectively for our IMACS and MDM photometry, and 0.06 and 0.14 magnitudes airmass^{-1} for our CTIO photometry.

$$I_{{\rm Inst},X} = I_{\rm Inst} - \alpha_I X_I \tag{2.2a}$$

$$V_{{\rm Inst},X} = V_{\rm Inst} - \alpha_V X_V \tag{2.2b}$$

To determine the average zero point offsets ($\langle B_I \rangle$,$\langle B_V \rangle$) between the SDSS transformed magnitudes ($I_{\rm SDSS}$,$V_{\rm SDSS}$) and our extinction-corrected instrumental magnitudes ($I_{{\rm Inst},X}$,$V_{{\rm Inst},X}$) we assumed a pair of linear relations between the two having the forms:

$$I_{\rm SDSS} = I_{{\rm Inst},X} + B_I \tag{2.3a}$$

$$V_{\rm SDSS} = V_{{\rm Inst},X} + B_V \tag{2.3b}$$

The plots in Figure 2.6 demonstrate these linear relationships for both filters and for each of the three IMACS photometric observing runs.

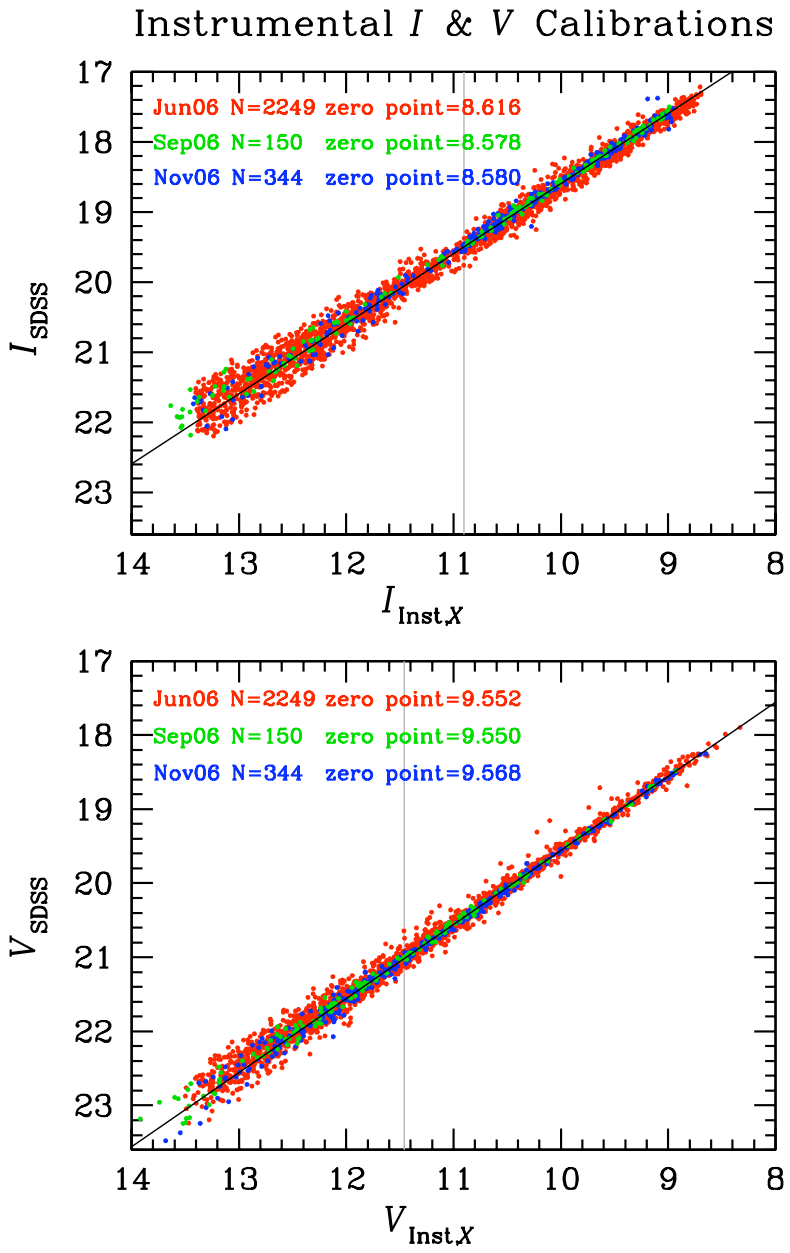

Figure 2.6: Photometric calibrations of instrumental I and V magnitudes. The calibrations of the airmass-corrected instrumental magnitudes was made using SDSS magnitudes that were converted to the Johnson-Cousins system. The different colored points represent stars from three different IMACS observing runs. To determine the zero point offsets for each run the average differentials $\langle I_{\rm SDSS} - I_{{\rm Inst},X} \rangle$ and $\langle V_{\rm SDSS} - V_{{\rm Inst},X} \rangle$ were calculated from the brightest 50% of the stars (designated by the light grey vertical line). The stars in the brightest half of the data set are mostly alignment candidates, while the fainter half are mostly Sgr candidates. The total number of stars and the zero point offset are given for each run. Although each of the three observing runs were fit separately, for clarity we plot a single best-fit line. All fields were normalized to the same exposure times to create this plot.

We then calculated the average offset for each filter and observing run ($\langle B_I \rangle$,$\langle B_V \rangle$) as the average difference between the magnitudes of SDSS and our instrumental magnitudes:

$$\langle B_I \rangle = \langle I_{\rm SDSS} - I_{{\rm Inst},X} \rangle \tag{2.4a}$$

$$\langle B_V \rangle = \langle V_{\rm SDSS} - V_{{\rm Inst},X} \rangle \tag{2.4b}$$

For the IMACS photometry, where the numbers of stars available to calibrate with are plentiful, only the the brightest half of the stars (as indicated in Figure 2.6) were used to calibrate with. Also, stars with highly discrepant residuals were iteratively rejected from the calibration. For our photometry from other instruments, stars of all brightnesses were used to calibrate, except those that were iteratively rejected. The only other significant difference in the calibration procedure based on the instrument used was that each of the seven operational CCDs of the 8K detector on the MDM 2.4 m needed to be calibrated independently because of large zero point offsets from chip to chip.

The final calibrated magnitudes (I, V) are then simply calculated as the extinction corrected instrumental magnitudes ($I_{{\rm Inst},X}$,$V_{{\rm Inst},X}$), plus the corresponding zero point offsets ($\langle B_I \rangle$,$\langle B_V \rangle$):

$$I = I_{{\rm Inst},X} + \langle B_I \rangle \tag{2.5a}$$

$$V = V_{{\rm Inst},X} + \langle B_V \rangle \tag{2.5b}$$

To correct for the effects of interstellar reddening, the galactic extinction (A_I,A_V),

as calculated from the maps of Schlegel et al. (1998), is subtracted from the final calibrated magnitudes (I, V):

$$I_0 = I - A_I \tag{2.6a}$$

$$V_0 = V - A_V \tag{2.6b}$$

Combining all terms, the dereddened final calibrated magnitudes (I_0,V_0) are calculated as the instrumental magnitudes ($I_{\rm Inst}$,$V_{\rm Inst}$), plus the zero point offsets ($\langle B_I \rangle$,$\langle B_V \rangle$), minus the effects of atmospheric extinction ($\alpha_I X_I$,$\alpha_V X_V$) and insterstellar reddening (A_I,A_V):

$$I_0 = I_{\rm Inst} + \langle B_I \rangle - \alpha_I X_I - A_I \tag{2.7a}$$

$$V_0 = V_{\rm Inst} + \langle B_V \rangle - \alpha_V X_V - A_V \tag{2.7b}$$

The residuals from these calibrations have rms values of 0.04–0.10 magnitudes in I and 0.04–0.08 magnitudes in V (when calculated using the brightest 50% of the stars) for the three IMACS observing runs. Figure 2.7 plots these residuals as a function of the corresponding instrumental magnitudes for the three IMACS photometric runs. We investigated the potential need to add a color term in to the calibration but found the residuals to be flat as a function of the calibrated color (see Figure 2.8), and determined none was necessary. We also chose to check that our calibrated colors are consistent with those reported by the SDSS. Figure 2.9 shows a pair of histograms of the differences between our calibrated colors and the colors from the SDSS for the same stars. We find the two to be in very good agreement, having average and median differences of just 0.01 magnitudes.

The dereddened, calibrated magnitudes for each object in our data set are presented in the field tables at the end of Chapter 3. The dereddened CMDs for all fields are provided at the end of this chapter (Figures 2.10 to 2.19).

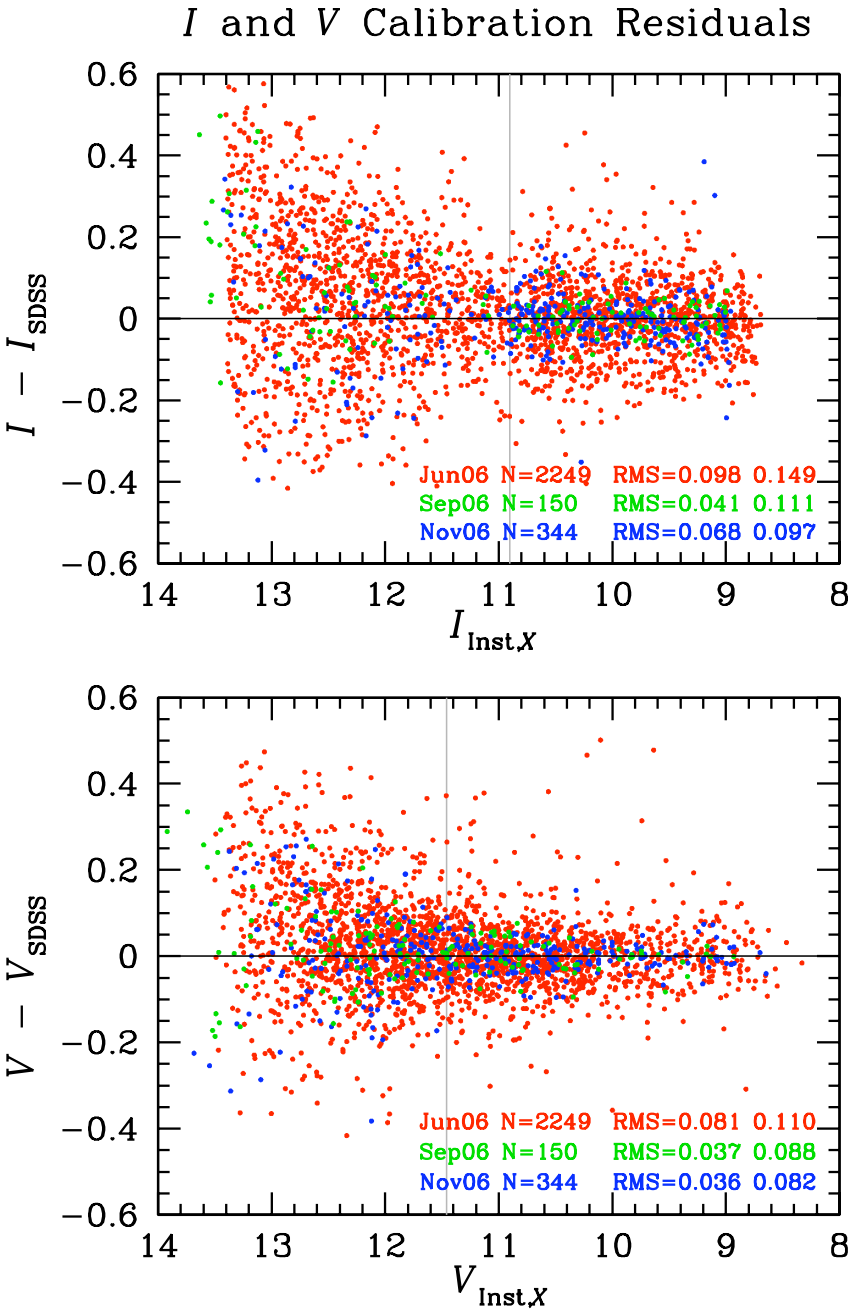

Figure 2.7: I and V band calibration residuals. The different colored points represent stars from three different IMACS observing runs. The light grey vertical lines separate the brightest 50% of the stars (which were used to determine the calibration) from the faintest 50%. The fainter star are mostly Sgr candidates while the brighter ones are mostly alignment candidates. The total number of stars from each observing run is shown along with the rms scatter of the brightest 50% of stars (first) and the entire sample (second). All fields were normalized to the same exposure times to create this plot.

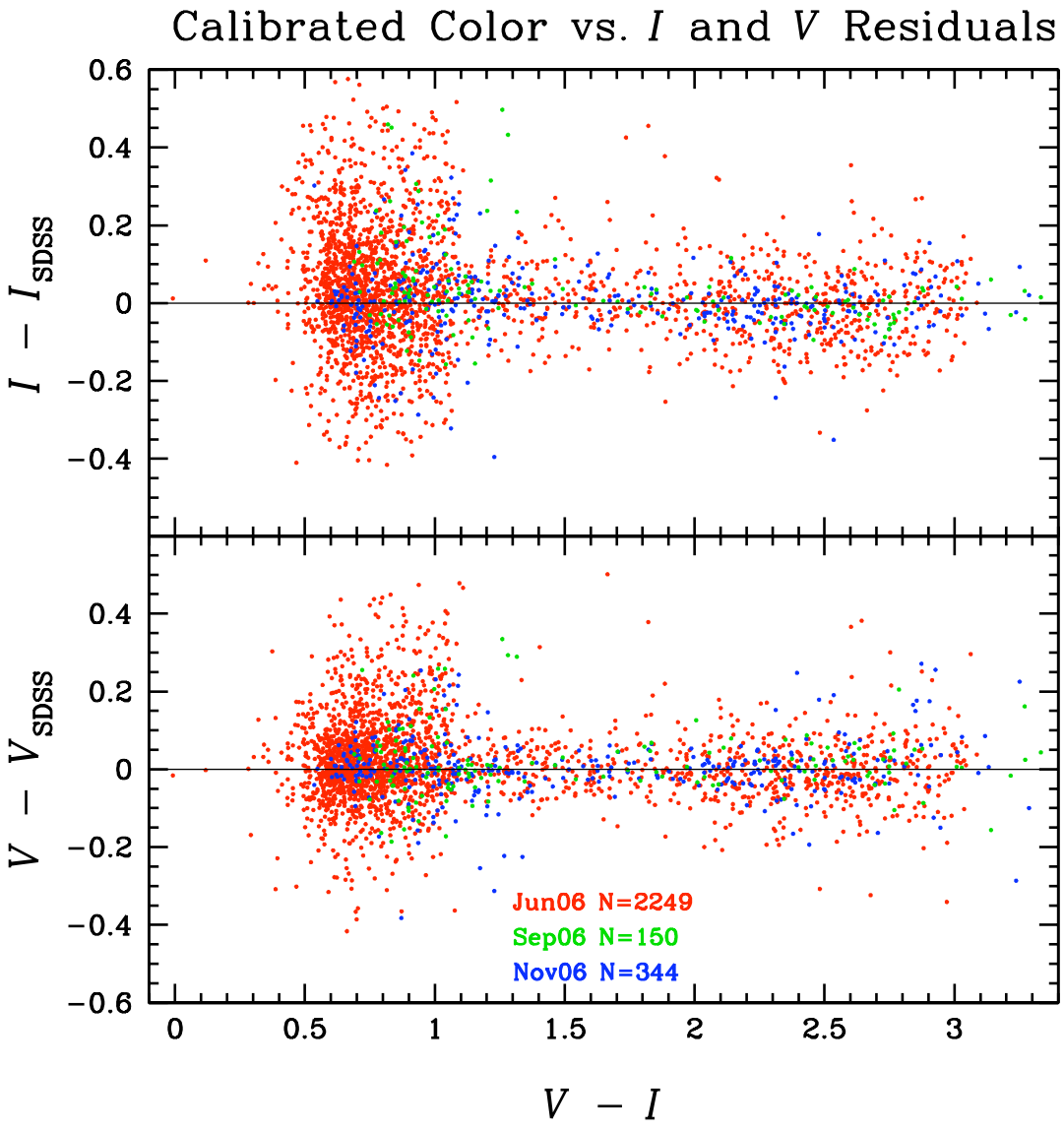

Figure 2.8: Calibrated $V-I$ color vs. I and V band residuals. The different colored points represent stars from three different IMACS observing runs. The total number of stars from each observing run is shown. The clump of stars centered at $V-I \sim 0.75$ is dominated by Sgr candidates, while the stars with $V-I \gtrsim 1.1$ are mostly alignment candidates. The lack of a discernible slope in either plot justifies the absence of a color term in our calibration equations.

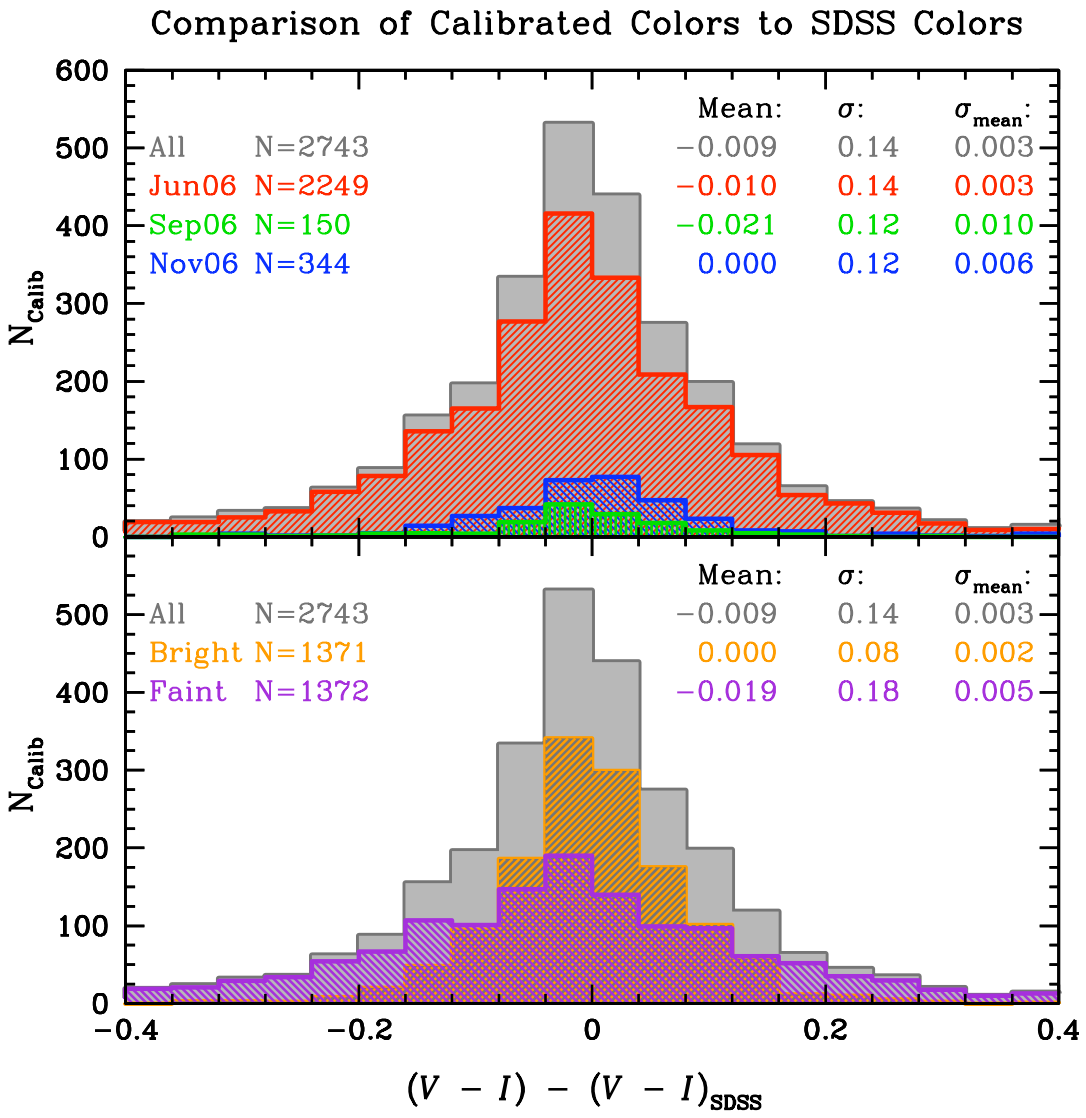

Figure 2.9: Comparison of calibrated colors to SDSS colors. The upper panel shows a histogram of the differences between our calibrated $(V - I)$ colors and those of the SDSS for each of the three IMACS oberving runs. The lower panel is a similar histogram but for the brightest 50% and faintest 50% of the stars. The bright subsample is mostly alignment candidates while the faint subsample is mostly Sgr candiates. While all five subsamples are centered at, or very close, to zero, the faint subsample is observed to have a significantly broader distribution, as one would expect for stars with higher photometric uncertainties. The number of stars in each subsample is provided, along with the mean, standard deviation, and the standard deviation of the mean.

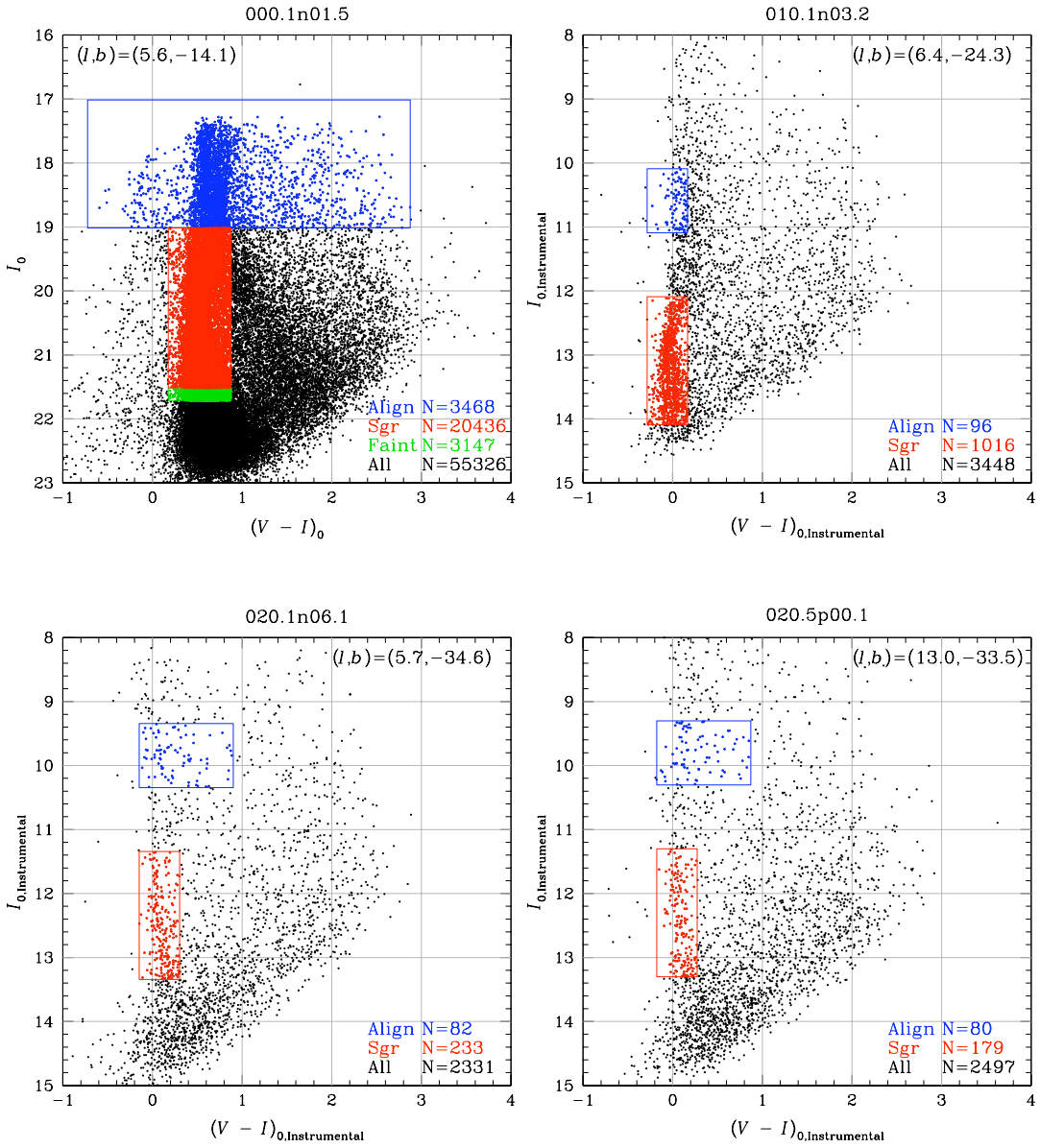

Figure 2.10: Dereddened color-magnitude diagrams of four fields. The red selection boxes indicate where our spectroscopic candidates were selected from. The blue selection boxes were used to select alignment stars for IMACS. The green selection boxes, where indicated, were used to select faint spectroscopic candidates to supplement the primary candidate list. The upper left field is the main body of Sagittarius. The other three fields were unable to be calibrated, so we plot their instrumental I magnitudes and $V - I$ colors.

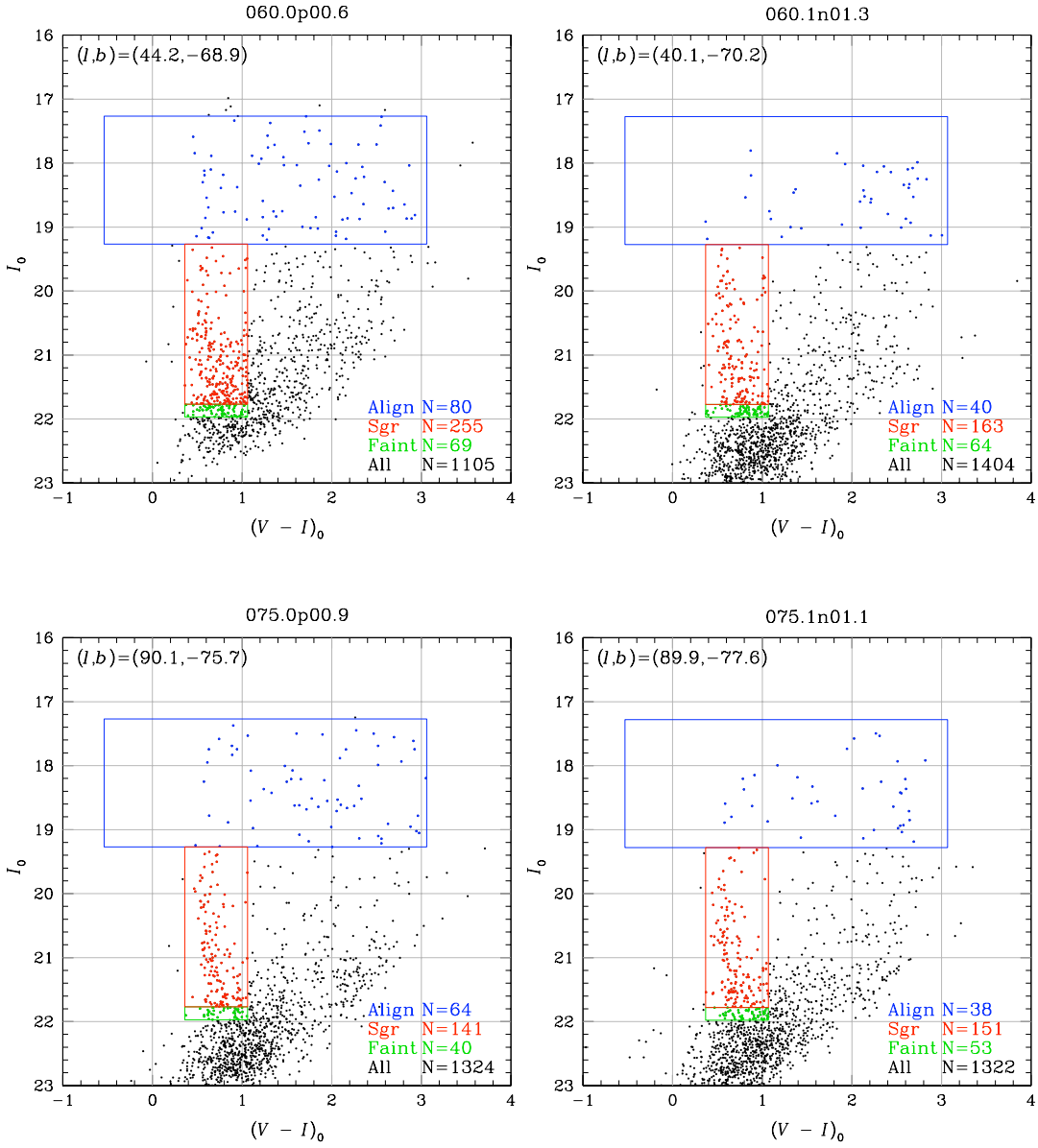

Figure 2.11: Dereddened color-magnitude diagrams of four fields. The red selection boxes indicate where our spectroscopic candidates were selected from. The blue selection boxes were used to select alignment stars for IMACS. The green selection boxes were used to select faint spectroscopic candidates to supplement the primary candidate list.

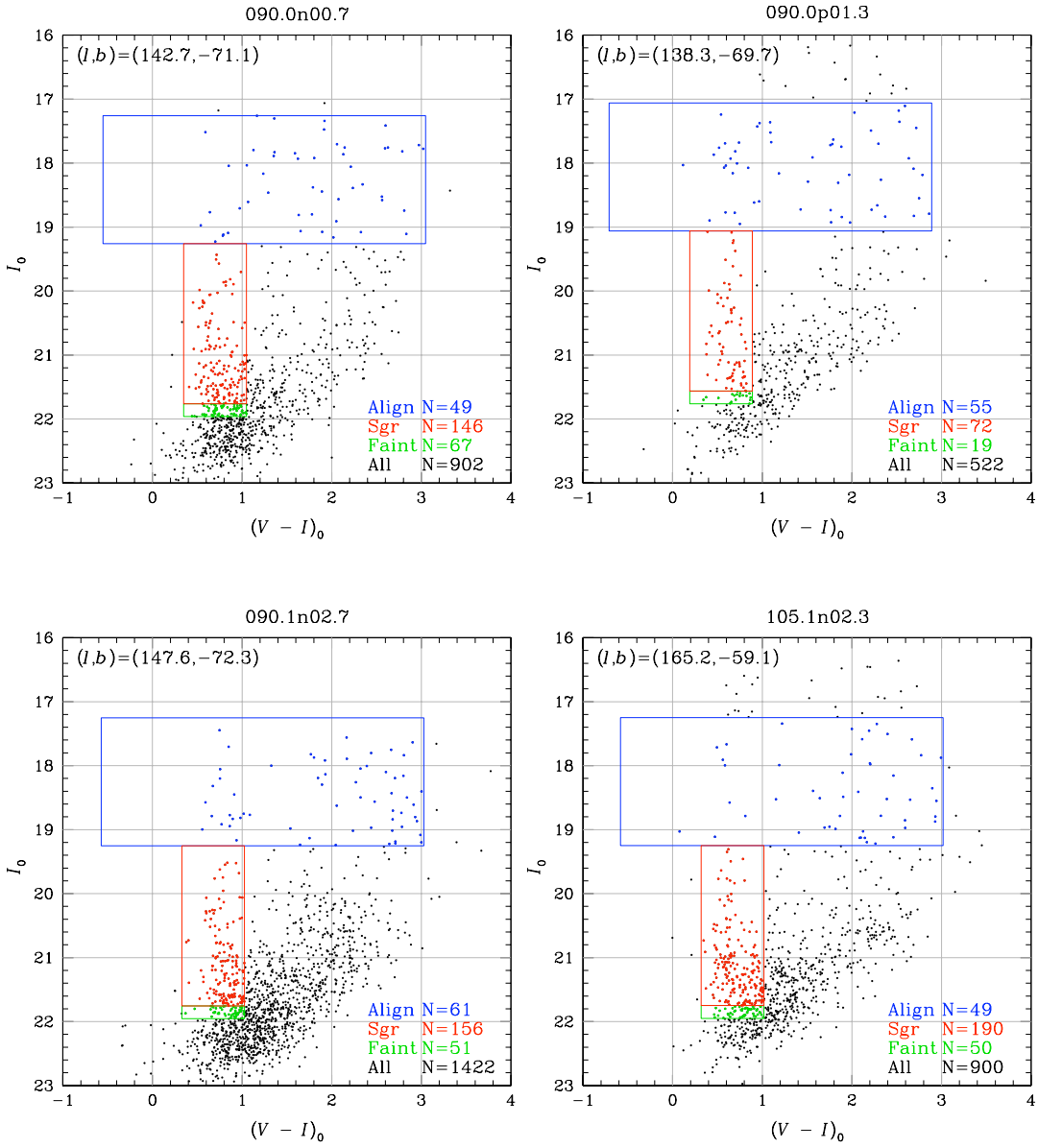

Figure 2.12: Dereddened color-magnitude diagrams of four fields. The red selection boxes indicate where our spectroscopic candidates were selected from. The blue selection boxes were used to select alignment stars for IMACS. The green selection boxes were used to select faint spectroscopic candidates to supplement the primary candidate list.

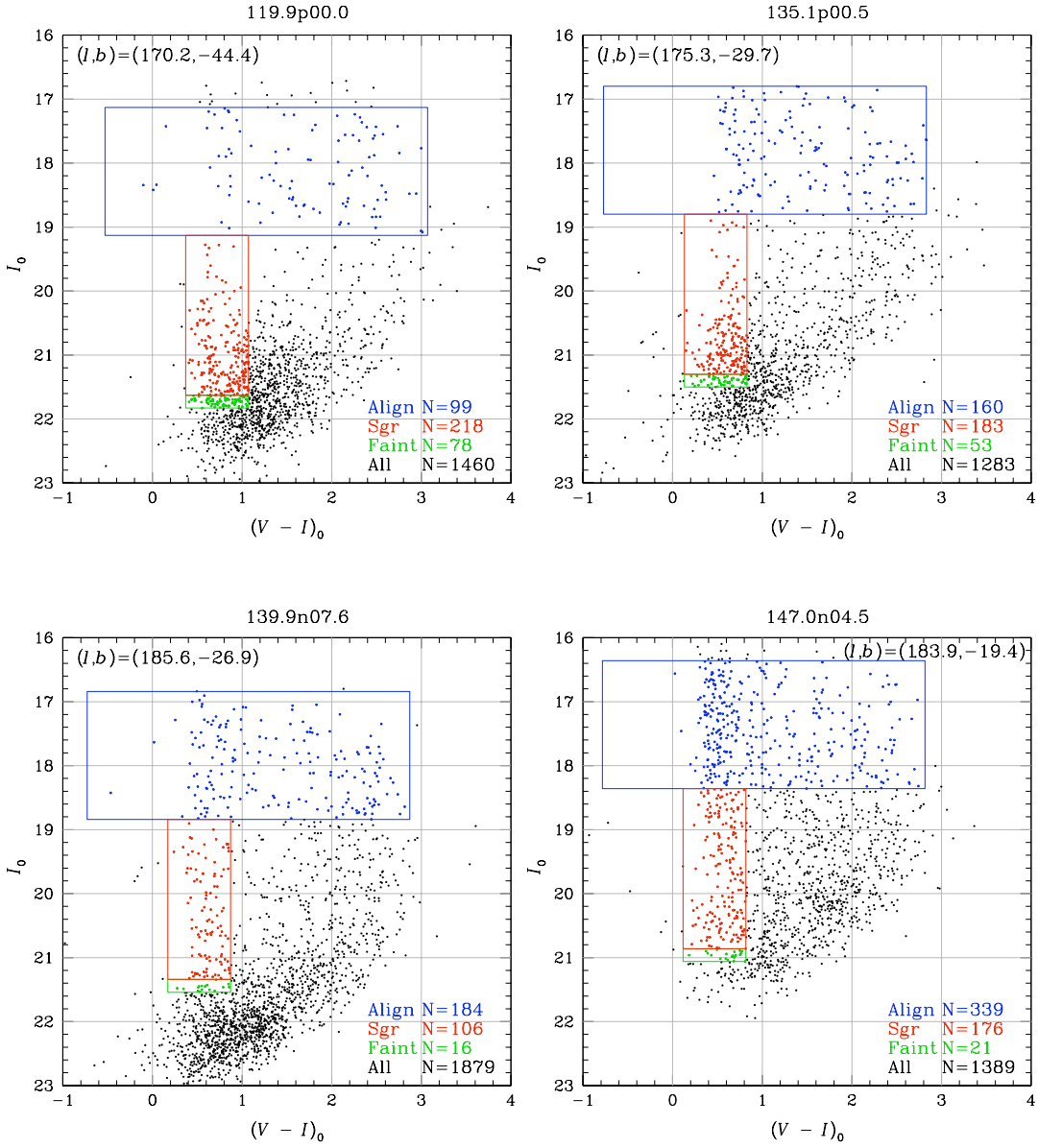

Figure 2.13: Dereddened color-magnitude diagrams of four fields. The red selection boxes indicate where our spectroscopic candidates were selected from. The blue selection boxes were used to select alignment stars for IMACS. The green selection boxes were used to select faint spectroscopic candidates to supplement the primary candidate list.

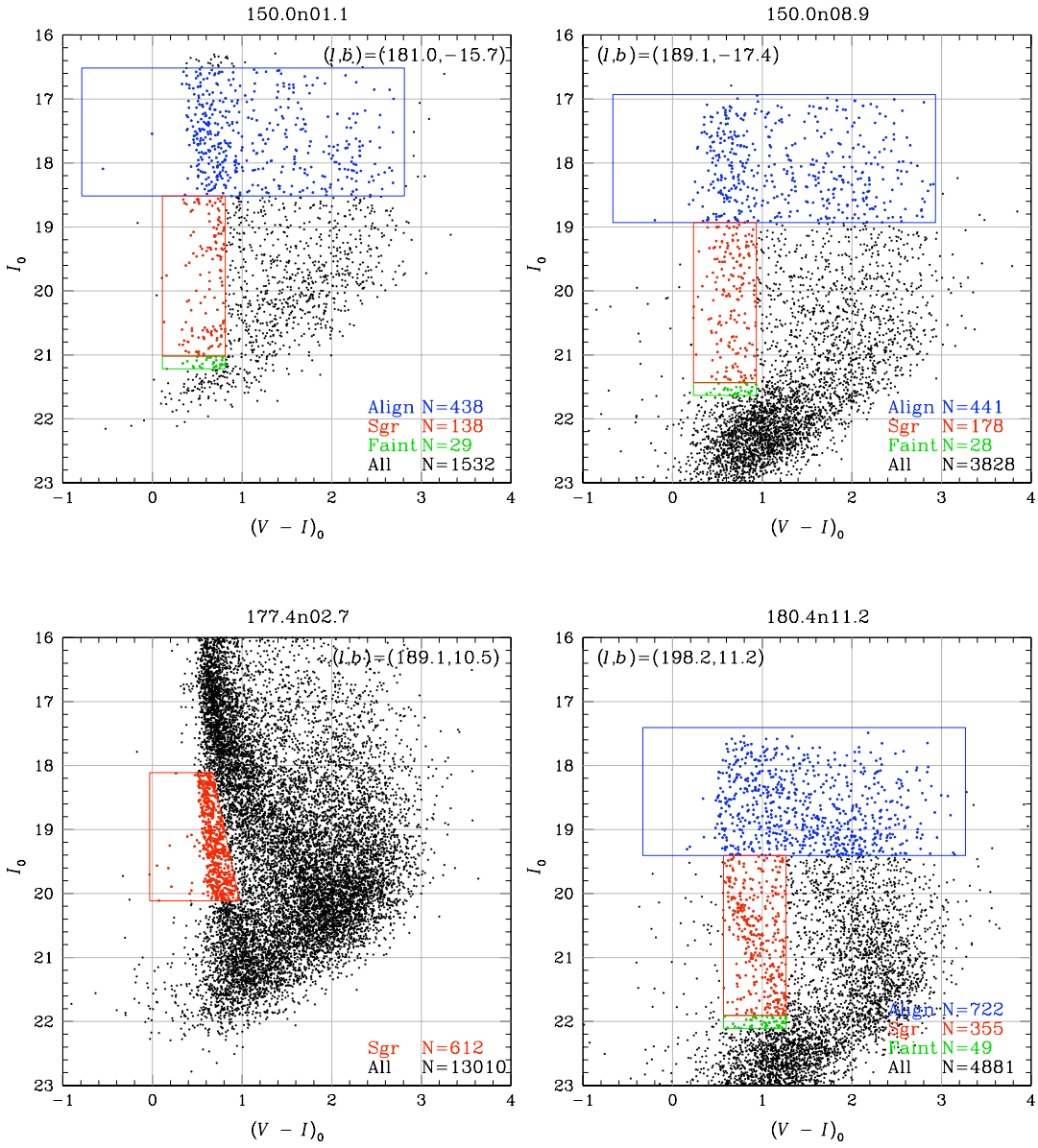

Figure 2.14: Dereddened color-magnitude diagrams of four fields. The red selection boxes indicate where our spectroscopic candidates were selected from. The blue selection boxes, where indicated, were used to select alignment stars for IMACS. The green selection boxes, where indicated, were used to select faint spectroscopic candidates to supplement the primary candidate list. Follow-up spectroscopy for the field in the lower left hand panel was done with Hectospec.

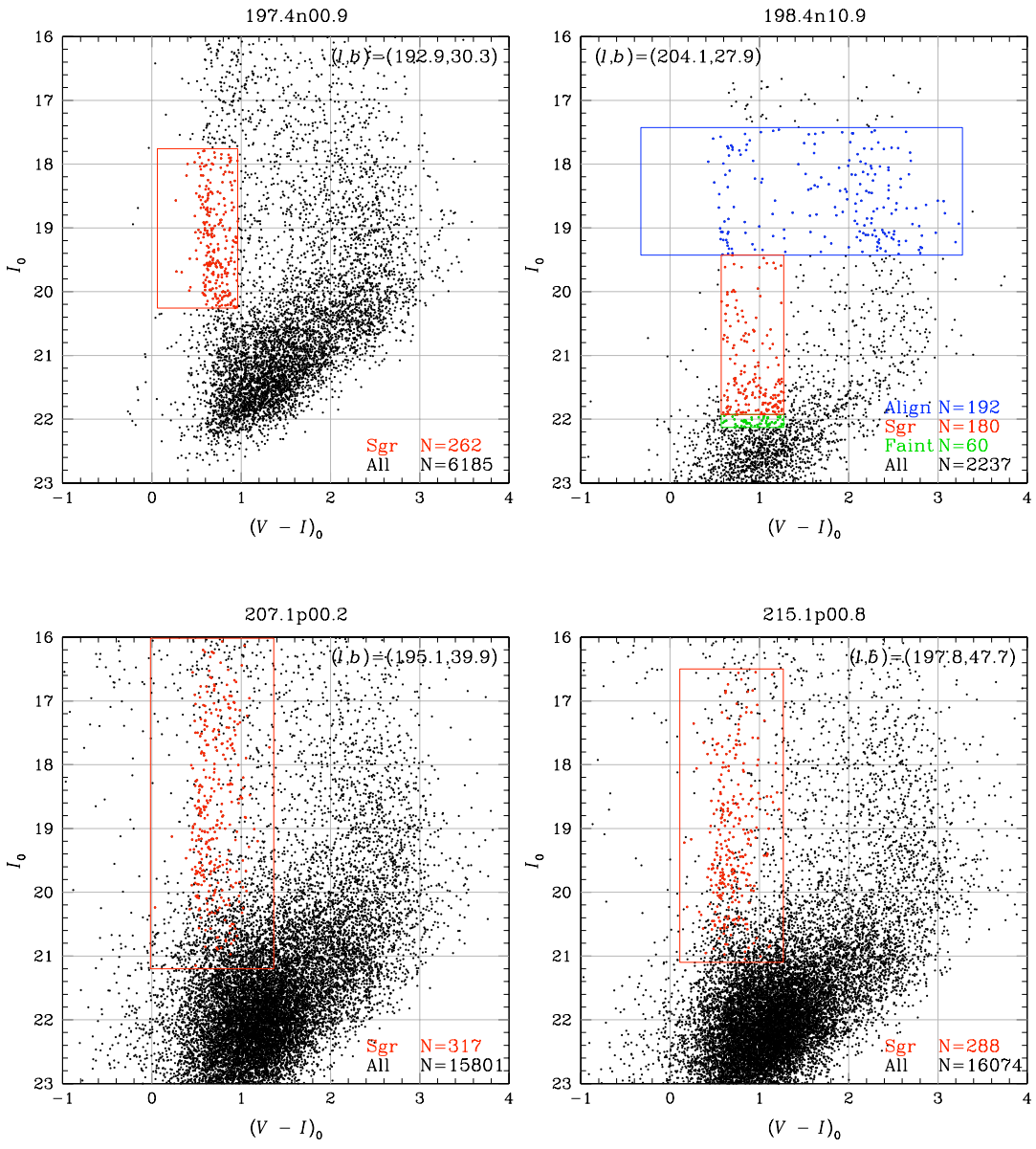

Figure 2.15: Dereddened color-magnitude diagrams of four fields. The red selection boxes indicate where our spectroscopic candidates were selected from. The blue selection boxes, where indicated, were used to select alignment stars for IMACS. The green selection boxes, where indicated, were used to select faint spectroscopic candidates to supplement the primary candidate list. The three fields with only red selection boxes were used to select candidates for follow-up spectroscopy with Hectospec. The lower two panels show some points colored as non-candidates within their selection boxes. These points were classified as non-candidates in the original uncalibrated CMDs that were used for selection. After applying chip-by-chip calibrations to the MDM 2.4m+8K, the points moved relative to one another, with some moving inside of the selection box.

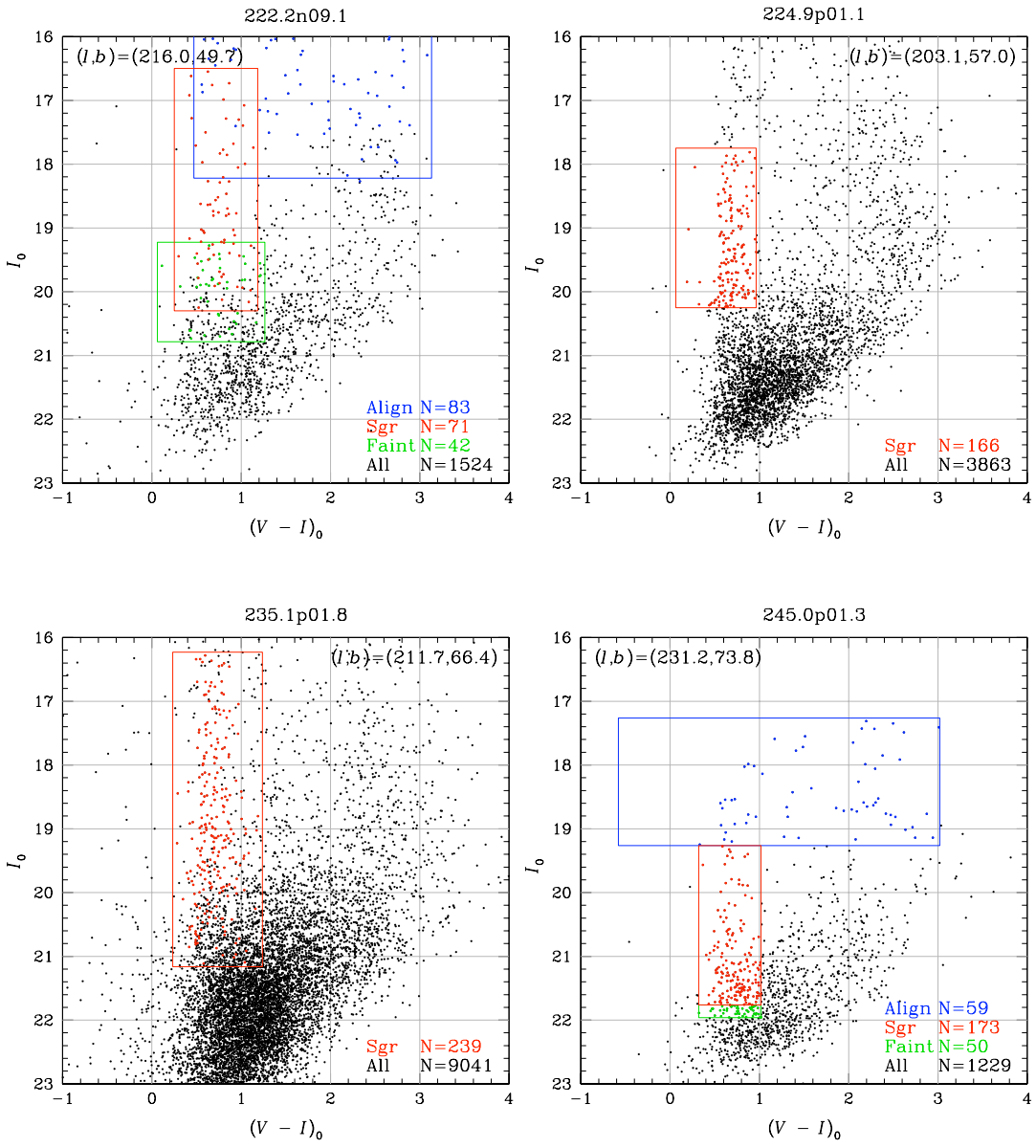

Figure 2.16: Dereddened color-magnitude diagrams of four fields. The red selection boxes indicate where our spectroscopic candidates were selected from. The blue selection boxes, where indicated, were used to select alignment stars for IMACS. The green selection boxes, where indicated, were used to select faint spectroscopic candidates to supplement the primary candidate list. Follow-up spectroscopy for the fields in the upper right and lower left hand panels was done with Hectospec. The field in the upper left hand panel with overlapping selection boxes was imaged with the MDM2.4m+8K. Candidates in that field were selected from uncalibrated CMDs. Each chip in the 8K CCD array needed to be calibrated independently, causing the points in the calibrated CMD to shift relative to one another when compared to the uncalibrated CMD. This resulted in overlapping selection boxes and points originally classified as non-candidates within the selection boxes.

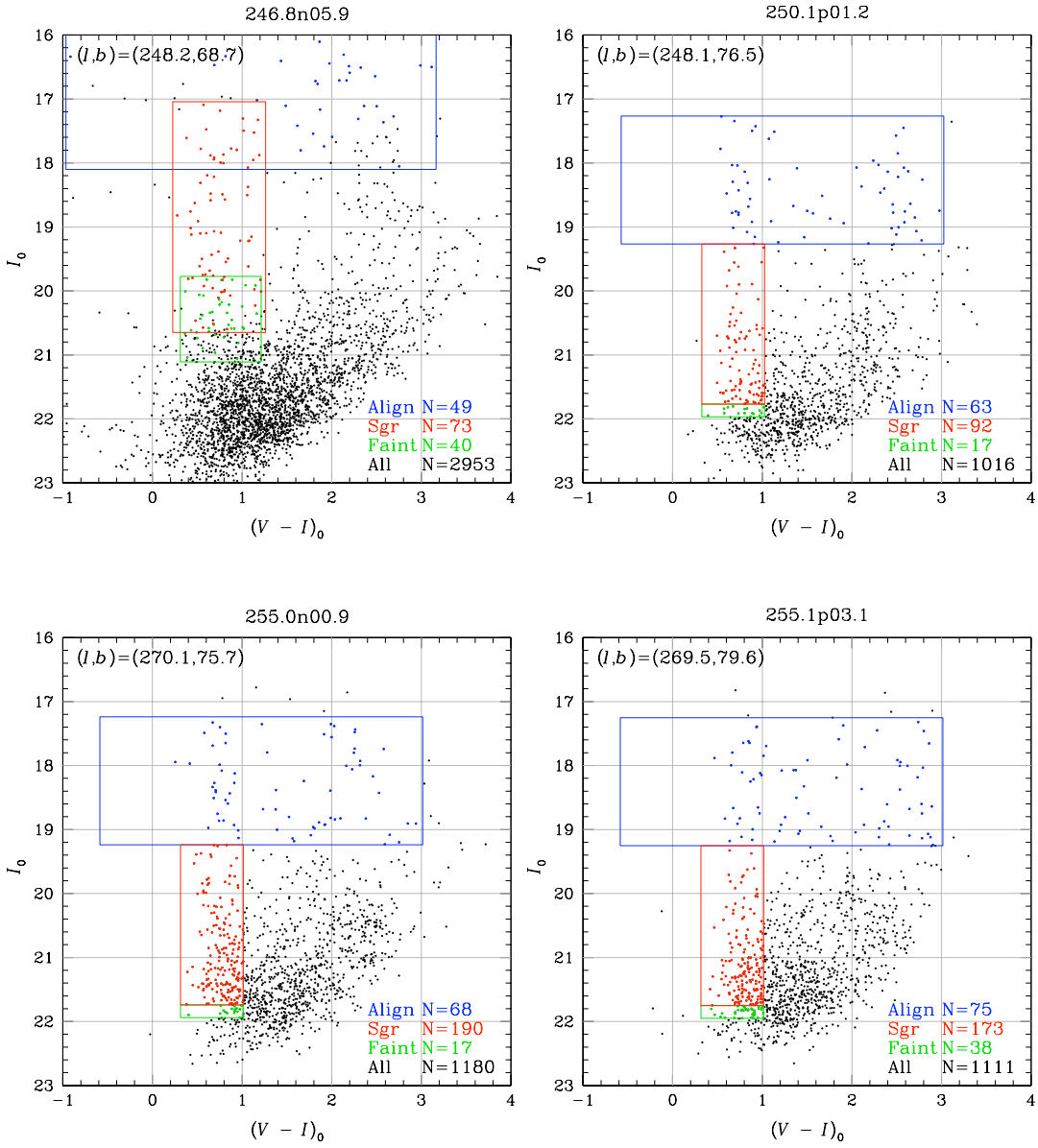

Figure 2.17: Dereddened color-magnitude diagrams of four fields. The red selection boxes indicate where our spectroscopic candidates were selected from. The blue selection boxes were used to select alignment stars for IMACS. The green selection boxes were used to select faint spectroscopic candidates to supplement the primary candidate list. For an explanation of the overlapping selection boxes in the upper left hand panel see the caption for the previous figure.

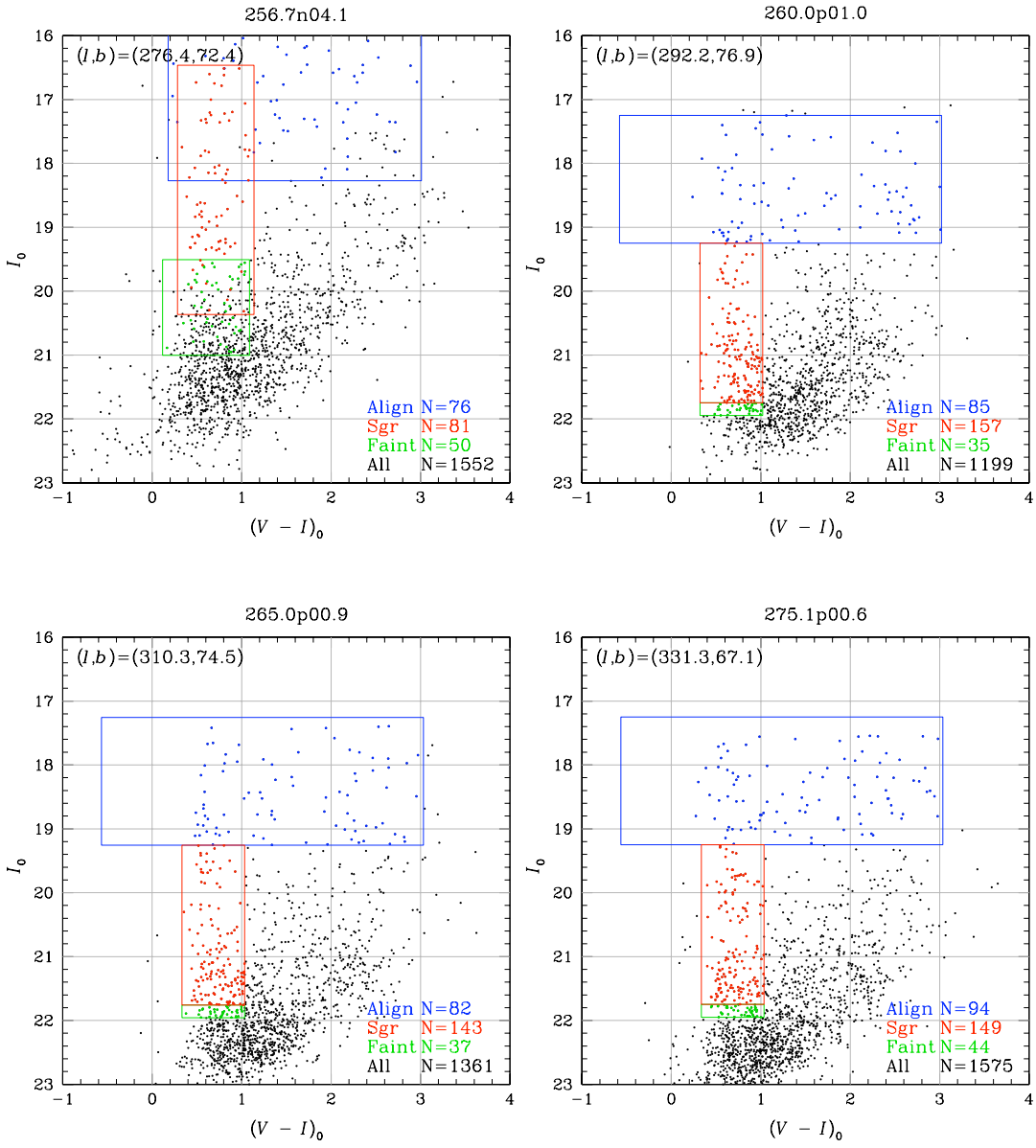

Figure 2.18: Dereddened color-magnitude diagrams of four fields. The red selection boxes indicate where our spectroscopic candidates were selected from. The blue selection boxes were used to select alignment stars for IMACS. The green selection boxes were used to select faint spectroscopic candidates to supplement the primary candidate list. For an explanation of the overlapping selection boxes in the upper left hand panel see the caption for figure 2.16.

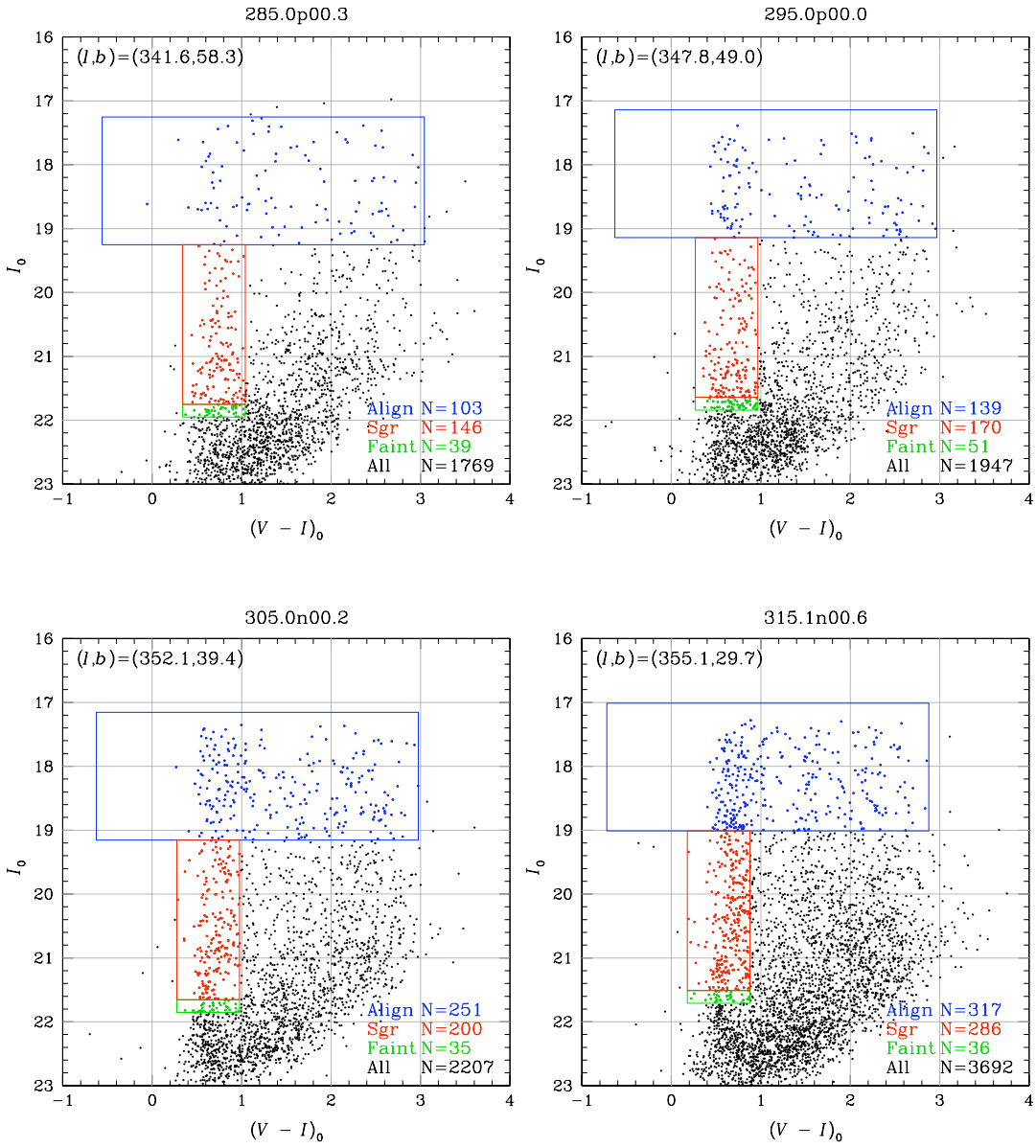

Figure 2.19: Dereddened color-magnitude diagrams of four fields. The red selection boxes indicate where our spectroscopic candidates were selected from. The blue selection boxes were used to select alignment stars for IMACS. The green selection boxes were used to select faint spectroscopic candidates to supplement the primary candidate list.